Spatially adaptive estimation of multi-layer soil temperature at a daily time-step across China during 2010-2020

Xuetong Wang[1, 2], Liang He[3, *], Peng Li[1, 2], Jiageng Ma[4], Yu Shi[5], Qi Tian[1, 2], Gang Zhao[2, 6], Jianqiang He[7], Hao Feng[2], Hao Shi[8, 9, *], Qiang Yu[2, *]

[1] College of Natural Resources and Environment, Northwest A&F University, Yangling 712100, China

[2] State Key Laboratory of Soil and Water Conservation and Desertification Control, Northwest A&F University, Yangling 712100, China

[3] National Meteorological Center, Beijing, 100081, China

[4] Key Laboratory of Ecosystem Network Observation and Modeling, Institute of Geographic Sciences and Natural Resources Research, Chinese Academy of Sciences, Beijing 100101, PR China

[5] Institute of Carbon Neutrality, Sino-French Institute for Earth System Science, College of Urban and Environmental Sciences, Peking University, Beijing 100871, China

[6] College of Soil and Water Conservation Science and Engineering, Northwest A&F University, Yangling, Shaanxi, 712100, China

[7] Key Laboratory for Agricultural Soil and Water Engineering in Arid Area of Ministry of Education, Northwest A&F University, Yangling 712100, China

[8] State Key Laboratory for Ecological Security of Regions and Cities, Research Center for Eco-Environmental Sciences, Chinese Academy of Sciences, Beijing, 100085, China

[9] College of Resources and Environment, University of Chinese Academy of Sciences, Beijing, 100049, China

Correspondence:

Liang He (heliang_hello@163.com)

Hao Shi (haoshi@rcees.ac.cn)

Qiang Yu (yuq@nwafu.edu.cn)

Abstract

Soil temperature (T_s) is critical in regulating agricultural production, ecosystem functions, hydrological cycling and climate dynamics. However, the inherent spatial and temporal heterogeneity of soil thermal regimes constitutes a persistent challenge in obtaining high-resolution, continuous gridded T_s datasets along vertical profiles. To address this issue, we propose a spatially adaptive layer-cascading Extreme Gradient Boosting (XGBoost) algorithm to generate daily multi-layer T_s data (0, 5, 10, 15, 20, and 40 cm) at a spatial resolution of 1 km in China from 2010 to 2020. The methodology dynamically partitions non-uniformly distributed measuring sites (2,093 sites across the country) to quadtrees and incorporates thermal coupling effects propagated between neighbor soil layers. Multi-source data, including satellite retrievals of land surface temperature and vegetation index, and ERA5 reanalysis climate variables were used as inputs. Validation using spatial block cross-validation and independent flux tower observations demonstrated the robustness and accuracy of the product.~~Independent tests demonstrated high robustness and accuracy of our model, with depth-specific values of coefficients of determination (R^2) being 0.94–0.98 and root mean square errors (RMSE) values ranging 1.75–2.21K.~~ It is noted the model's performance was lower in summers and winters than in springs and autumns. Compared to existing global or regional T_s products, the dataset developed here is characterized by its fine spatio-temporal patterns and high reliability, enabling it to provide supports for precision agriculture, ecosystem modeling and understanding climate-land feedback. Free access to the dataset can be found at https://doi.org/10.11888/Terre.tpdc.302333 ~~–~~(Wang et al., 2025b)~~(X. Wang et al., 2025)~~.

Key words: Soil temperature, spatially adaptive, machine learning, multi-source data

设置了格式: 字体颜色: 蓝色

1. Introduction

Soil temperature (T_s) is a critical driver of ecosystem dynamics, influencing nearly all physical, chemical, and biological processes (Bayatvarkeshi et al., 2021; Xu et al., 2023; Liu et al., 2025). T_s plays a pivotal role in land-atmosphere exchanges. By controlling the partitioning of net radiation into sensible and latent heat fluxes, T_s directly shapes atmospheric boundary layer circulation, with cascading effects on regional climate patterns (Mahanama et al., 2008; Chen et al., 2021a). T_s also drives soil freeze-thaw cycles, which are critical for hydrological processes in cold regions. Permafrost thaw alters subsurface water storage, runoff dynamics and groundwater recharge, with implications for both local and basin-scale hydrology (Zhang et al., 2005; Shati et al., 2018). In addition, it governs the rates of soil microbial activities, nutrient cycling, and organic matter decomposition, with direct implications for carbon dynamics. For instance, T_s modulates microbial respiration, thereby regulating the release of organic carbon into the atmosphere as CO_2 that is central to global carbon cycling (Yang et al., 2011). Given its multifaceted influences on carbon cycling, climate feedbacks and hydrological systems, accurate T_s estimation is indispensable for advancing ecosystem monitoring, refining climate models, and developing effective strategies to mitigate and adapt to climate change.

T_s exhibits high heterogeneity at large spatial scales due to varying driving factors. Solar radiation changes its radiation intensity by adjusting the incident angle and sunshine duration, thus affecting the heating effects on surface soils (Wang and Dickinson, 2013). Additionally, diurnal variations of air temperature cause periodic changes in surface temperature, while the amplitude is often closely related to the local climate and topography. Furthermore, surface covers (e.g., vegetation and snow) significantly impact T_s (Xu et al., 2020; Mortier et al., 2024). Vegetation canopies effectively intercept and scatter solar radiation, while root systems modulate soil

moisture distribution, thereby stabilizing deeper soil temperatures (Li et al., 2024). Snow cover, characterized by high albedo, reflects substantial solar radiation and acts as an effective insulator, mitigating cold air penetration and maintaining warmer soil temperatures during winter months (Myers-Smith et al., 2015). Moreover, thermal conductivity and heat capacity are critical parameters controlling vertical heat transfer in soils. Sandy soils have higher porosity and lower water retention, resulting in lower heat capacity and higher thermal conductivity, thus responding rapidly to temperature changes. In contrast, clay soils have lower porosity and stronger water retention, leading to higher heat capacity and significant thermal stability, characterized by delayed responses to temperature variations (Ochsner et al., 2001; Zhao et al., 2022). Understanding these mechanisms is essential for developing refined vertical T_s distribution models and improving the accuracy of T_s estimation.

Given these complex processes, accurately estimating T_s across different depths is challenging. Quite a few models have been proposed for T_s estimation. These models can be generally classified into physical, statistical or empirical, and machine learning (ML) types (Li et al., 2024; Farhangmehr et al., 2025). Physical models, derived from fundamental heat conduction laws and energy balance equations, provide explicit mechanistic interpretations but suffer from computational complexity and heavy reliance on multi-domain input parameters, which range from soil properties to climatic variables (Gao et al., 2008; Hu et al., 2016; Badache et al., 2016). Statistical or empirical models, such as autoregressive integrated moving average and regression methods (Xing et al., 2018), are usually limited to localized, small-sample applications. Data-driven ML~~machine learning~~ techniques demonstrate a superior ability to capture nonlinear relationships and thus usually can obtain high prediction accuracy. For instance, at site scale, Feng et al. (2019) estimated multi-layer T_s at half-hourly resolutions using Extreme Learning Machine, with a RMSE ranging from 2.26~2.95 K. Li et al., (2022) implemented an attention-aware long short-term memory (LSTM) model for predicting next-day T_s and the model obtained a RMSE of 0.74~2.53 K. At the regional scale, Xu et al. (2023) integrated satellite remote sensing with a deep belief

设置了格式: 字体颜色: 蓝色

network model to reconstruct continuous T_s profiles (at depths of 5–40 cm) across the Qinghai-Tibetan Plateau (QTP), obtaining $R^2 > 0.836$ and MAE < 2.152 °C. Similarly, Farhangmehr et al. (2025) developed a hybrid convolutional neural network-LSTM (CNN-LSTM) architecture for predicting T_s across North American climatic zones at 0–7 cm depths, with R^2 ranging from 0.93 to 0.99.

Although significant advances have been made in estimating T_s, large-scale T_s prediction continues to confront critical challenges, sourcing from environmental complexity and methodological limitations. First, T_s exhibits considerable spatial heterogeneity driven by regional disparities in topography, soil composition, vegetation density, and microclimate (Bayatvarkeshi et al., 2021). These factors create nonstationary relationships between T_s and explanatory variables (e.g., air temperature, soil moisture), necessitating regionally tailored modeling approaches. Second, data scarcity and uneven spatial distribution of site measurements introduce further complexity. Aggregating sparse, unevenly distributed measurements into a single model often leads to overfitting: high accuracy on training data but poor generalization to underrepresented regions or previously unseen data (Li et al., 2024). Ultimately, developing models that reconcile scalability (for large spatial scales) with localized precision (to capture site-specific interactions) remains an unresolved priority, underscoring the persistent challenge of balancing universal applicability with spatially adaptive fidelity in T_s prediction methodology.

To address the above challenges, this study proposes a spatially adaptive methodology based on quadtrees. This approach dynamically partitions the study area into grids of varying sizes, with smaller grids in densely observed regions and larger grids in sparsely sampled areas, thereby enabling localized modeling that better captures spatial heterogeneity across complex environmental gradients. In addition, multi-source environmental predictors are integrated, and XGBoost models are applied within each grid cell to capture the nonlinear relationships between T_s and its driving factors. Importantly, we employ a spatial block cross-validation strategy to evaluate the model's generalization ability in unseen regions. Based on this framework, the

设置了格式: 字体颜色: 黄色
设置了格式: 非突出显示
设置了格式: 非突出显示

objectives of this study are to: (1) construct a spatially adaptive modeling system; (2) generate a multi-layer T_s dataset at a daily time-step and one kilometer resolution in China from 2010-2020; and (3) evaluate the dataset through independent validation with flux tower observations and benchmarking against widely used T_s products. The proposed methodology could directly address the scaling challenges induced by spatial heterogeneity and uneven data distribution. The generated products would provide a robust foundation for high-resolution environmental modeling, precision agriculture and climate impact assessments.

~~In this study, we propose a spatial scale-adaptive methodology based on quadtrees for multi-layer T_s estimation. The objectives are to: (1) develop a novel modeling framework by integrating multi-source data, including in-situ observations, remote sensing products, meteorological variables, and auxiliary environmental data; (2) generate a multi-layer T_s dataset at a daily time-step and one kilometer resolution in China from 2010-2020; and (3) assess the accuracy of the dataset through independent validation and benchmarking against widely used T_s products. The proposed methodology could explicitly address the scaling challenges induced by spatial heterogeneity and uneven data distribution. The generated products would provide a robust foundation for high-resolution environmental modeling, precision agriculture and climate impact assessments.~~

设置了格式: 字体颜色: 蓝色

带格式的: 缩进: 首行缩进: 0 字符

2. Materials and methods

2.1 In-situ T_s observations

In this study, in-situ T_s observations was measured at six depths: at the surface (0 m), and at subsurface levels of 0.05, 0.10, 0.15, 0.20, and 0.40 meters. Data were collected through the national weather station network operated by the China Meteorological Administration (CMA), in accordance with standardized measurement protocols. At each site, T_s was recorded every 10 minutes and automatically uploaded to a central server. Daily mean values at each depth were calculated from these high-frequency records. We then assessed data completeness for the period 2010–2020 and

设置了格式: 字体颜色: 蓝色

设置了格式: 字体颜色: 蓝色

excluded stations with more than 20% missing daily records at any depth. After quality control, 2,093 stations were retained for model development. ~~In this study, in-situ T_s observations were sourced from the China Meteorological Administration, encompassing daily mean T_s data collected from 2,093 stations across the period 2010–2020. These stations recorded T_s at six standard soil depths: 0, 5, 10, 15, 20, and 40 cm.~~

The observation network spans a wide range of climatic zones—from cold and temperate to subtropical and tropical, and includes diverse land-use and ecosystem types, such as forests, grasslands, croplands, and barren lands. However, the spatial distribution of stations is notably uneven. High station density is observed in northeastern China, the central and eastern plains, and the southern hilly regions, whereas station coverage is sparse in the arid and semi-arid regions of northwestern China and on the QTP. The spatial distribution of in-situ observation sites is shown in Figure 1, and details of the dataset partitioning strategy are provided in Section 2.3.3. ~~Figure.1 illustrates the spatial configuration of the dataset: gray dots represent samples used for model training, while red dots denote those reserved for model testing. Details regarding the dataset partitioning strategy are provided in Section 2.3.3.~~

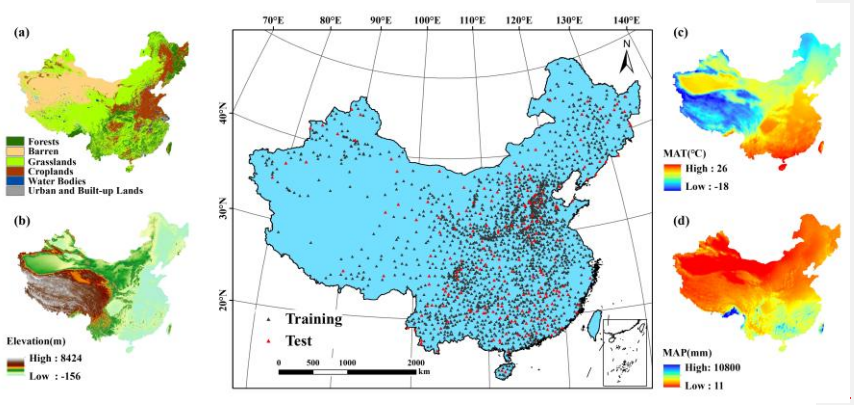

设置了格式: 字体颜色: 蓝色

设置了格式: 字体: 非加粗, 字体颜色: 蓝色

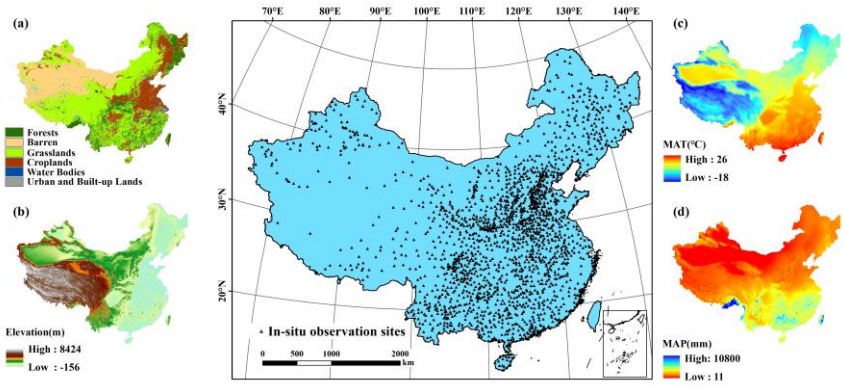

Figure 1. Spatial distribution of in-situ T_s sites at different depths across China and the corresponding environmental variables. This figure presents the spatial distribution of 2,093 in-situ T_s sites across China~~, with samples divided into the training set (gray) and the test set (red)~~. The environmental variables corresponding to these sites include (a) land cover types (forests, barren land, grasslands, croplands, water bodies, and urban areas), (b) elevation (ranging from -156 m to 8424 m), (c) mean annual temperature (MAT, ranging from -18°C to 26°C), and (d) mean annual precipitation (MAP, ranging from 11 mm to 10,800 mm).

2.2 Predictor variables

To construct a robust multi-layer T_s estimation model, we selected a comprehensive suite of predictor variables, integrating remote sensing products, meteorological factors, and auxiliary environmental data. Meteorological variables, especially air temperature and precipitation, have been consistently recognized in previous studies as primary determinants of T_s variability (Bond-Lamberty et al., 2005; Nahvi et al., 2016). Among these, air temperature has been widely regarded as the most influential variable due to its strong linear relationship with T_s (Khosravi et al., 2023).

In addition, both net solar radiation and downward longwave radiation (LWD) were considered. Net solar radiation directly represents the shortwave energy absorbed by the land surface and serves as the primary driver of the daytime surface energy budget, whereas LWD plays a particularly important role under nighttime and winter conditions by regulating surface heat loss through the longwave radiation balance. Together, they jointly control the surface energy balance and directly drive the spatiotemporal dynamics of T_s (Peng et al., 2016)~~. In addition, solar radiation was~~

设置了格式: 字体颜色: 蓝色

设置了格式: 字体颜色: 蓝色

~~included, given its significant role in regulating the surface energy balance through its influence on net radiation, latent heat flux, and ground heat flux, all of which directly affect T_s dynamics.~~

Thermal infrared remote sensing data also exhibit a high correlation with near-surface T_s. Integrating thermal remote sensing products and energy balance-based models offers an effective means of estimating T_s with high spatial and temporal continuity. This strategy has been validated by numerous studies (Huang et al., 2020; Xu et al., 2023). Surface land cover further modulates T_s by altering surface albedo, regulating evapotranspiration (ET), and influencing energy partitioning processes. Accordingly, the enhanced vegetation index (EVI), derived from satellite observations, was incorporated as a proxy for vegetation density and type (Bright et al., 2017; Li et al., 2024b). To capture the influence of underlying surface characteristics on T_s, topographic variables such as elevation and slope were included, along with soil texture data across various depths. These features collectively reflect the heterogeneous physical and thermal properties of the soil, contributing to spatial variations in heat conduction and storage capacity. A full list of the predictor variables used in the model is summarized in Table 1.

Table 1. Details of the predictor variables for training the model.

Type	Data	Variable	Spatial resolution	Temporal resolution	Reference
Remotely sensed product	MOD09GA	EVI	500 m×500 m	Daily	Huete et al., 2002
	MOD11A1	LST_ Day	1 km×1 km	Daily	
	MOD11A1	LST_ Night	1 km×1 km	Daily	
Climate data	ERA5-Land	Temperature_2m	9 km×9 km	Daily	Muñoz-Sabater et al., 2021
		surface_net_solar_radiation_sum~~Solar_radiation~~			
		surface_thermal_radiation_downwards_sum			
		Precipitation			
		~~Wind_10m~~			
Supplementary	USGS_STRM	Elevation	30 m		

设置了格式: 字体: (中文) +中文正文 (等线)

设置了格式: 字体颜色: 蓝色

设置了格式: 字体: (中文) +中文正文 (等线)

data		Slope	30 m		
	Soil Texture	Sand, Silt, Clay Depth: 0-5, 5-15, 15-30, 30-60cm	250 m×250 m		Liu et al., 2022
	In-situ measurements	Soil temperature at 0, 5, 10, 15, 20, and 40 cm	-	Daily	

2.2.1 Remote sensing data

The MOD11A1 LST product, at a daily time-step and a spatial resolution of 1 km, was utilized. It includes both daytime (LST_{day}) and nighttime (LST_{night}) temperatures at 10:30 AM and 10:30 PM, respectively, along with quality assessment information (Wan and Dozier, 1996). To enhance the estimation of daily mean T_s, the average of LST_{day} and LST_{night} values was calculated and used in the analysis.

EVI from 2010 to 2020 were selected as predictor of T_s. The MODIS Surface Reflectance Product (MOD09GA), derived from MODIS Level-1B data, provides daily surface reflectance of seven bands at 500 m × 500 m resolution. The EVI is defined by Huete et al., (2002), and the retrieval equation is as follows:

$$EVI = G \times \frac{\left(\rho_{SR\_b1} - \rho_{SR\_b2}\right)}{\left(\rho_{SR\_b1} + C_1 \times \rho_{SR\_b2} - C_2 \times \rho_{SR\_b3} + L\right)} \quad (1)$$

where G = 2.5, C_1 = 6, C_2 = 7.5, L = 1. The remote sensing reflectance variables *SR_b1*(620-670nm), *SR_b2* (841-876nm) and *SR_b3* (459–479 nm) of MOD09GA data represents red, near-infrared and blue bands. The coefficients 2.5 and 1 represent the gain and canopy background, respectively (Huete et al., 2002). The atmospheric influence on the red band is corrected using the blue band and the coefficients 6 and 7.5, respectively.

Subsequently, cloud contamination caused partial spatial absences in the daily LST and EVI. To address this issue, we applied a temporal and spatial linear interpolation algorithm, which utilizes time-series data from adjacent days and spatial information from neighboring pixels to fill the current missing values, thereby generating a time-continuous and spatially complete image series. This approach follows the methods

described in Chen et al., (2017) and Cao et al., (2018), with modifications to better suit our dataset. Then, the Savitzky-Golay (S-G) filter was used to smooth the interpolated data, resulting in continuous surface temperature and vegetation index data with high temporal and spatial resolution (Kong et al., 2019; Chen et al., 2021b). All data preprocessing, including image filtering and interpolation, was conducted within the Google Earth Engine (GEE) platform.

2.2.2 Climate data

The ERA5-Land is the fifth-generation reanalysis dataset produced by the European Centre for Medium-Range Weather Forecasts (ECMWF). It assimilates multi-source data, including weather station measurements, numerical weather predictions, and satellite observations, into dynamic models to generate reanalysis data (Muñoz-Sabater et al., 2021). It provides high-quality environmental variables related to water and energy fluxes between the land surface and atmosphere, with continuous coverage from 1981 to the present. ERA5-Land offers a spatial resolution of 0.1° (~9 km at the equator) and an hourly temporal resolution, making it well-suited for modeling near-surface processes. In this study, we extracted daily mean values of key climate variables, including 2-meter air temperature (Temperature_2m), surface solar radiation ~~,~~and total precipitation~~, and 10-meter wind speed (wind_speed_10m),~~ from the ERA5-Land Daily dataset. All variables were accessed and processed using the GEE platform.

带格式的: 缩进: 首行缩进: 2 字符

2.2.3 Auxiliary data

Topographic and soil-related variables were incorporated as auxiliary predictors to improve the accuracy of T_s estimation. Elevation and slope were derived from the Shuttle Radar Topography Mission (SRTM) digital elevation model (Farr et al., 2007), specifically using the Version 3 (SRTM Plus) product with a spatial resolution of 1 arc second (~30 m). Soil texture plays a critical role in determining T_s through its influence on thermal conductivity, which is affected by physical properties such as particle size

distribution, porosity, bulk density, and moisture retention capacity. In this study, we represented soil texture using the relative proportions of clay (fine), silt (medium), and sand (coarse) particles. To capture vertical variability in soil properties, we employed the China Soil Information Grid dataset developed by Liu et al. (2022), which provides gridded estimates of soil composition at four depth intervals: 0–5 cm, 5–15 cm, 15–30 cm, and 30–60 cm. The dataset offers a spatial resolution of 1 km and is suitable for high-resolution, profile-based soil modeling.

2.3 Methods

The spatial adaptive modeling framework consists of three modules as shown in Fig. 3. Module I is for data collection and preprocessing, which mainly involves in-situ observations, remote sensing, meteorological and supplementary data. Module II is spatial adaptive modeling, which mainly includes the construction of rotated quadtrees and local modeling based on XGBoost. Finally, module III is the layer-to-layer reconstruction of daily 1km resolution multi-layer (0, 5, 10, 15, 20, and 40 cm) T_s datasets in China from 2010 to 2020.

2.3.1. Feature selection

Multicollinearity among multiple source variables may affect the robustness of the models. Therefore, we rigorously evaluated the multicollinearity among the independent variables using the variance inflation factor (VIF) before modeling to remove highly correlated variables. The VIF is a diagnostic statistic used to quantify the degree of multicollinearity by measuring how much the variance of a regression coefficient is inflated due to correlations with other predictors~~To mitigate multicollinearity among predictor variables, we calculated the Variance Inflation Factor (VIF) for all candidate features(Akinwande et al., 2015) (Akinwande et al., 2015)(Akinwande et al., 2015).~~ (Akinwande et al., 2015). It is calculated as:

$$VIF_i = \frac{1}{1-R_i^2} \quad (2)$$

带格式的: 缩进: 首行缩进: 2 字符

带格式的: 缩进: 首行缩进: 2 字符

设置了格式: 字体颜色: 蓝色

设置了格式: 字体颜色: 蓝色

设置了格式: 字体颜色: 蓝色

设置了格式: 字体颜色: 着色 5

设置了格式: 字体颜色: 着色 5

带格式的: 缩进: 首行缩进: 0.35 厘米

域代码已更改

where R_i^2 is the coefficient of determination obtained by regressing the i-th predictor against all other predictors. Variables with VIF exceeding 10 are generally considered severely multicollinear and should be removed.

Based on the VIF analysis, we applied the following adjustments to the predictor set. Accordingly, some variables were excluded due to severe multicollinearity or redundancy. Specifically, sand, silt, and clay are compositional variables whose proportions sum to 100%, leading to perfect collinearity. To reduce redundancy, we removed silt while retaining sand and clay. In addition, LWD was found to be highly correlated with net solar radiation at the daily mean scale (Fig. S1) and was therefore excluded from the final modeling.

In contrast, although the daily mean LST (LST_mean) and air temperature also exhibited strong collinearity, with VIF values exceeding 10 (Fig. S2), we decided to retain both. This decision reflects their physical distinctness and complementary information: LST_mean provides higher spatial resolution (1 km), whereas air temperature offers broader meteorological consistency (9 km). Such differences are particularly important in complex ecosystems such as forests, where canopy structure and biological processes substantially influence thermal dynamics (Liu et al., 2025).~~As shown in Fig. S1, both the daily mean LST (LST_mean) and air temperature exhibited high collinearity, with VIF values exceeding 10. Although LST_mean offers higher spatial resolution (1 km) compared to air temperature (9 km), it is crucial to recognize that these two variables are physically distinct. Their differences become particularly pronounced in complex ecosystems such as forests, where canopy structure and biological processes significantly influence thermal dynamics (Liu et al., 2025). Given these considerations, both LST_mean and air temperature were retained for the estimation of Ts at the 0 cm depth, as they offer complementary information. Following feature selection, all retained variables were resampled to a common spatial resolution of 1 km using bilinear interpolation to ensure consistency in subsequent modeling steps.~~

2.3.2. Spatial adaptive partition of site measurements

设置了格式: 字体: 小四, 字体颜色: 蓝色
设置了格式: 字体: 小四, 字体颜色: 蓝色
设置了格式: 字体: 小四, 字体颜色: 蓝色
域代码已更改
域代码已更改
设置了格式: 字体颜色: 蓝色
设置了格式: 字体: 小四, 字体颜色: 蓝色
带格式的: 缩进: 首行缩进: 2 字符
设置了格式: 非突出显示
设置了格式: 非突出显示
设置了格式: 字体颜色: 蓝色
带格式的: 缩进: 首行缩进: 2 字符

A quadtree is a hierarchical spatial data structure that recursively subdivides a two-dimensional space into four quadrants, enabling efficient spatial indexing and localized data organization. In this study, we adopted a bottom-up, rotated quadtree-based spatial partitioning strategy that adaptively generates finer grids in regions with dense samples and coarser grids in sparse regions. Compared to global modeling or static grid partitioning, this adaptive approach offers improved regional modeling fidelity while significantly enhancing computational efficiency. The procedure consists of the following steps:~~A quadtree is a hierarchical spatial data structure that recursively subdivides a two-dimensional space into four quadrants, enabling efficient spatial indexing and localized data organization. In this study, we adopted a rotated quadtree-based spatial partitioning strategy to facilitate region-specific T_s modeling. The procedure comprises the following steps:~~

(1) Initialization of Minimum Units

The entire spatial domain was first divided into uniform, minimum-sized units (leaf nodes), each representing a fundamental spatial element. These units may contain zero or more in-situ observations. This initial step provides the base resolution for subsequent hierarchical construction. The structure and principle of quadtree spatial indexing are illustrated in Fig. S3~~2~~.

(2) Hierarchical Merging

~~Beginning with the leaf nodes, neighboring quadrants (i.e., groups of four adjacent nodes) were recursively merged into parent nodes if they satisfied a specified threshold: each sub-node contained fewer than 30 observational sites. This criterion ensures a balance between regional modeling precision and sample size sufficiency. The merging process continued upward through the hierarchy until no further aggregation met the threshold. The resulting partitions define spatially adaptive subregions, each of which is assigned a localized T_s prediction model.~~Starting from the leaf nodes, groups of four adjacent quadrants were recursively merged into parent nodes if each contained fewer than 30 observation sites (threshold selection detailed in Fig. S4). The merging process

设置了格式: 字体颜色: 着色 5

设置了格式: 字体颜色: 着色 5

设置了格式: 字体颜色: 蓝色

设置了格式: 字体颜色: 蓝色

设置了格式: 字体颜色: 蓝色

continued upward until no further groups met the threshold. This approach ensures that each node has sufficient sample size while achieving spatially adaptive partitioning across the study area. Each subregion is then assigned a localized T_s prediction model.

(3) Rotation at different angles

To reduce~~address~~ potential edge effects introduced by static grid boundaries, we implemented a rotated quadtree partitioning strategy. The quadtree structure was rotated at six angles (0°, 15°, 30°, 45°, 60°, and 75°), producing distinct sets of spatial partitions for each orientation (Fig. 2). Independent models were trained for each rotated configuration, and the final T_s estimates were obtained by averaging the outputs from all six models. This rotation-based ensemble method improves spatial smoothness and minimizes discontinuities at partition boundaries~~This rotational ensemble approach enhances spatial continuity and reduces boundary artifacts in the final predictions~~.

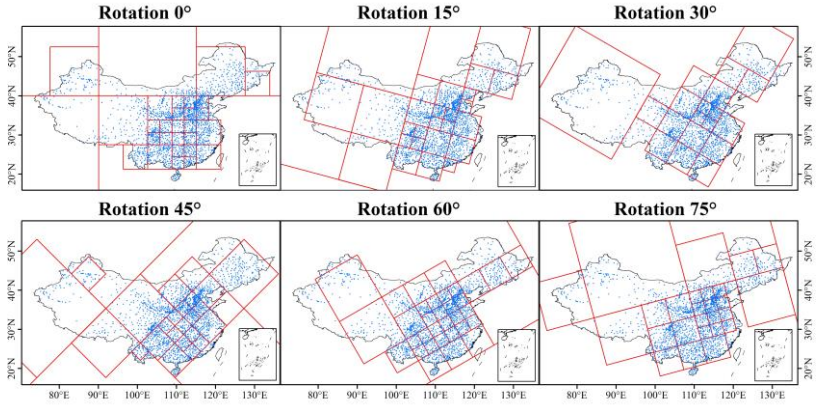

Figure 2. multi-angle adaptive quadtree partitioning of site observations (0°, 15°, 30°, 45°, 60°, 75°)

2.3.3. Machine learning algorithm

~~We selected the XGBoost (Extreme Gradient Boosting) algorithm for T_s estimation due to its proven accuracy, computational efficiency, and scalability for large-scale regression tasks. Introduced by (Chen and Guestrin, 2016), XGBoost constructs an ensemble of regression trees in a sequential manner, where each new tree is trained to~~

设置了格式: 字体颜色: 蓝色
设置了格式: 字体颜色: 蓝色
设置了格式: 字体颜色: 文字 2
设置了格式: 字体颜色: 蓝色
设置了格式: 字体颜色: 蓝色
设置了格式: 字体颜色: 蓝色

~~correct the residuals of the preceding ones. This iterative boosting process continues until convergence criteria are met, and the final prediction is obtained by aggregating the outputs of all trees. Compared to other machine learning algorithms such as support vector machines, random forests, and neural networks, XGBoost offers optimized performance through parallel computing, efficient memory usage, and a second-order gradient descent optimization strategy that accelerates training. Its robustness and predictive power have been widely demonstrated in geoscience and remote sensing applications, including land surface temperature reconstruction (Li et al., 2024) and multi-layer soil moisture estimation (Karthikeyan and Mishra, 2021).~~We adopted the XGBoost (Extreme Gradient Boosting) algorithm as the core regression model for T_s estimation due to its strong predictive performance, computational efficiency, and scalability across large environmental datasets. XGBoost constructs an ensemble of regression trees in a stage-wise boosting process, where each successive tree is trained to minimize the residuals of the previous iteration, thereby producing a robust and optimized model (Chen and Guestrin, 2016). One of the key strengths of XGBoost is its ability to handle heterogeneous and high-dimensional predictor sets, which are common in geoscience applications involving complex terrain, land cover variability, and climatic gradients. Recent studies have demonstrated its effectiveness in similar domains, including land surface temperature reconstruction (Li et al., 2024), multi-layer soil moisture estimation (Karthikeyan and Mishra, 2021), drought event attribution (Wang et al., 2025a)~~(Zhang et al., 2025)~~, and crop yield prediction (Li et al., 2023b). Given these proven strengths and the spatially nonstationary characteristics of T_s in our study area, XGBoost was selected to train localized prediction models within spatial subregions.

~~As shown in Fig. 3, (Chen and Guestrin, 2016)the observational dataset was stratified into training (70%), validation (20%), and test (10%) subsets through random sampling. A separate XGBoost model was constructed for each spatial grid using the Python XGBoost package(Chen and Guestrin, 2016). To prevent overfitting, model hyperparameters were carefully tuned. Specifically, we optimized key parameters~~

设置了格式: 字体颜色: 蓝色
设置了格式: 字体颜色: 蓝色
设置了格式: 字体颜色: 蓝色
设置了格式: 字体颜色: 蓝色
设置了格式: 字体颜色: 蓝色
设置了格式: 字体颜色: 蓝色
设置了格式: 字体颜色: 蓝色
设置了格式: 字体颜色: 蓝色
设置了格式: 字体颜色: 蓝色
设置了格式: 字体颜色: 蓝色
设置了格式: 字体颜色: 蓝色
带格式的: 缩进: 首行缩进: 0 字符

~~including the number of trees (n_estimators), maximum tree depth (max_depth), and learning rate (eta). GridSearchCV was applied to conduct an exhaustive search over the hyperparameter space defined in Table S1. Five-fold cross-validation was used to evaluate model generalizability and identify the optimal hyperparameter combinations for each local model.~~

To rigorously account for the strong spatial autocorrelation of T_s and avoid potential data leakage between training and testing subsets, we employed a spatial block cross-validation scheme rather than random splitting. Specifically, within each rotated quadtree grid, observation sites were grouped into spatial blocks based on their geographic coordinates: station latitude and longitude were each divided by 1° and floored to integer values, and stations sharing the same index were assigned to the same block. This ensured that samples within the same spatial block were not simultaneously assigned to both the training and testing subsets, thereby avoiding data leakage due to spatial autocorrelation and enabling a more reliable evaluation of the model's generalization capability.

Within each spatial grid, the data were partitioned into training (90%) and testing (10%) subsets at the block level. The training subset was further subjected to 10-fold spatial block cross-validation using GridSearchCV to optimize three key hyperparameters: the number of trees (n_estimators), maximum tree depth (max_depth), and learning rate (learning_rate). Detailed parameter settings are provided in Appendix Table S1. The hyperparameter set that yielded the lowest average validation error across the ten folds was selected as optimal. The final model was retrained on the full training set with the optimized parameters and evaluated on the held-out testing set to assess generalization.

A layer-wise prediction strategy was adopted to estimate T_s along the soil profile. For the surface layer (0 cm), predictors included air temperature and daily mean LST. For subsurface layers, these two variables were replaced by the T_s estimate from the immediately preceding layer, enabling the model to capture vertical heat conduction

processes and thereby improving the continuity and physical consistency of layer-wise T_s estimation~~allowing the model to account for vertical temperature conduction processes and improving the continuity of layer-wise T_s estimation~~.

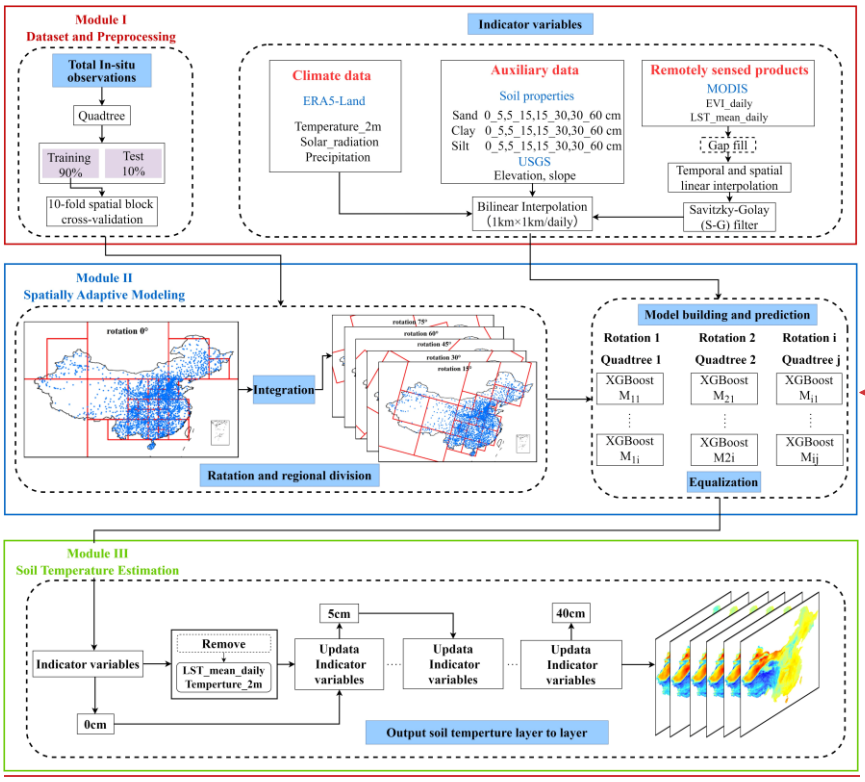

带格式的: 缩进: 首行缩进: 0 字符

设置了格式: 字体颜色: 蓝色

带格式的: 居中, 缩进: 首行缩进: 0 字符

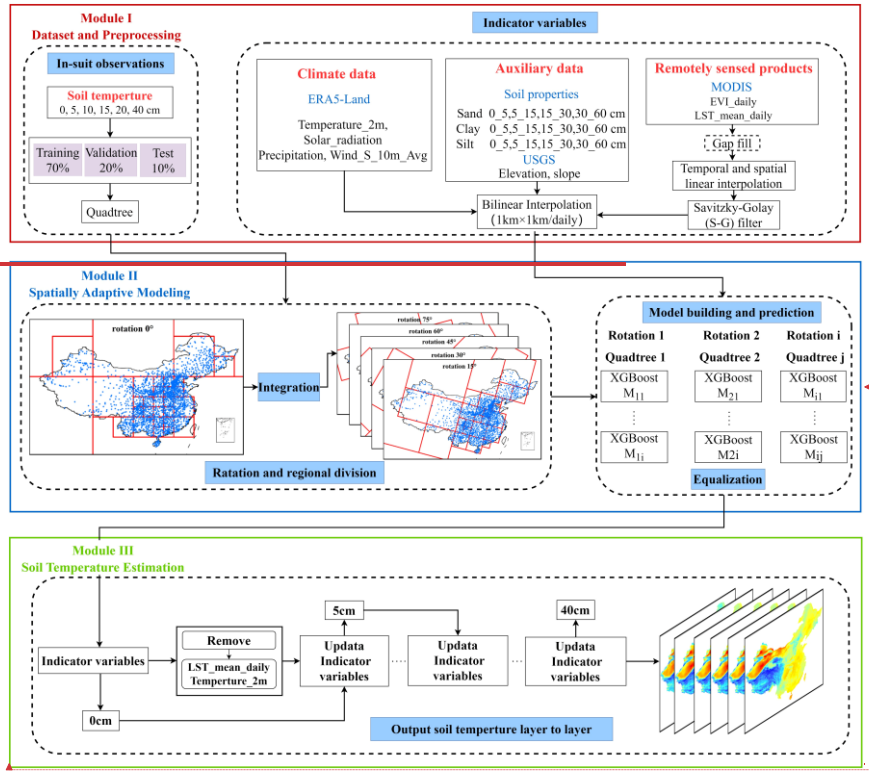

Figure 3. Workflow of the proposed method to obtain multi-layer T_s over the China.

2.3.4. Model evaluation metrics

The modeling performance and quality of the predicted T_s were evaluated in terms of RMSE, Mean Absolute Error (MAE), R^2, and Bias. RMSE and MAE were used to assess the ability to estimate volatility and fluctuation amplitude, respectively. R^2 represented the percentage of variance explained by the ML models. Bias was used to determine whether the estimations were overestimated or underestimated. These metrics were computed as follows:

$$RMSE = \sqrt{\frac{\sum_{i=1}^{N}[(x_i - \overline{X}) - (y_i - \overline{Y})]^2}{N}} \quad (32)$$

$$MAE = \frac{\sum_{i=1}^{N}|x_i - y_i|}{2} \quad (43)$$

设置了格式: 字体颜色: 蓝色
带格式的: 居中
带格式的: 缩进: 首行缩进: 0 字符, 行距: 1.5 倍行距
带格式的: 居中, 行距: 1.5 倍行距
设置了格式: 字体颜色: 着色 5
设置了格式: 字体颜色: 着色 5
设置了格式: 字体颜色: 着色 5

$$Bias = \frac{1}{N}\sum_{i=1}^{N}(x_i - y_i) \quad (54)$$

$$R^2 = 1 - \frac{\sum_{i=1}^{N}(y_i - x_i)^2}{N\sum_{i=1}^{N}(y_i - \overline{Y})^2} \quad (65)$$

where y_i and x_i denoted the in-situ T_s and estimated T_s for all the stations and periods, respectively. $\overline{Y}$ and $\overline{X}$ represented the mean values of the in-situ T_s and estimated T_s, respectively.

3. Results

3.1 Model performance across sites

Figure 4 illustrates the accuracy performance of all models constructed at various depths, utilizing different grid configurations and rotation angles, for both the training and ~~validation~~test sets. The grouped box plots demonstrate that the R^2 values for the training and test ~~validation~~ sets at different depths range from 0.82 to 0.98, and the RMSE values vary from 0.6 to 2.8 K. Both the training and test ~~validation~~ sets exhibit high accuracy with no evident signs of overfitting. A depth-wise comparison shows that model performance at 0 cm and 40 cm is marginally lower than at other depths.

Furthermore, to enhance the independence of the evaluation, we validated the final dataset against daily T_s observations from 18 flux tower sites of the ChinaFLUX network. For consistency, we retained measurements only at depths of 0, 5, 10, 15, 20, and 40 cm. Metadata for these sites is provided in Table S2, and the corresponding validation results are presented in Figure 5. The evaluation shows that our dataset achieves high accuracy at these independent sites (R^2 = 0.85–0.90; RMSE = 3.3–4.2 K), further demonstrating the robustness of our approach. Taken together, the validation results from both spatial block cross-validation and flux tower observations confirm that the spatially adaptive model we developed exhibits reliable accuracy and strong spatial generalization capability.~~Additionally, we evaluated the model's performance at~~

设置了格式: 字体颜色: 着色 5
设置了格式: 字体颜色: 着色 5
设置了格式: 字体颜色: 着色 5
设置了格式: 字体颜色: 着色 5
设置了格式: 字体颜色: 着色 5
设置了格式: 字体颜色: 着色 5
设置了格式: 字体颜色: 蓝色

~~different depths using an independent dataset comprising 210 sampling sites. Final predictions at each site were obtained by averaging the outputs from six rotations. Figure 5 presents scatter density plots comparing the predicted results with in-situ observations. The results at all depths are close to the 1:1 reference line. The R^2 values for different depths range from 0.93 to 0.97, and RMSE values between 1.74 and 2.25 K. Although the validation accuracy at depths of 0 cm and 40 cm is marginally lower than at 5, 10, 15, and 20 cm, the independent validation results across all depths demonstrate excellent overall performance. Overall, the accuracy validation results from the model's training set, validation set, and independent sample points indicate that the spatially adaptive model we developed has robust accuracy and strong generalization capability.~~

设置了格式: 字体颜色: 蓝色

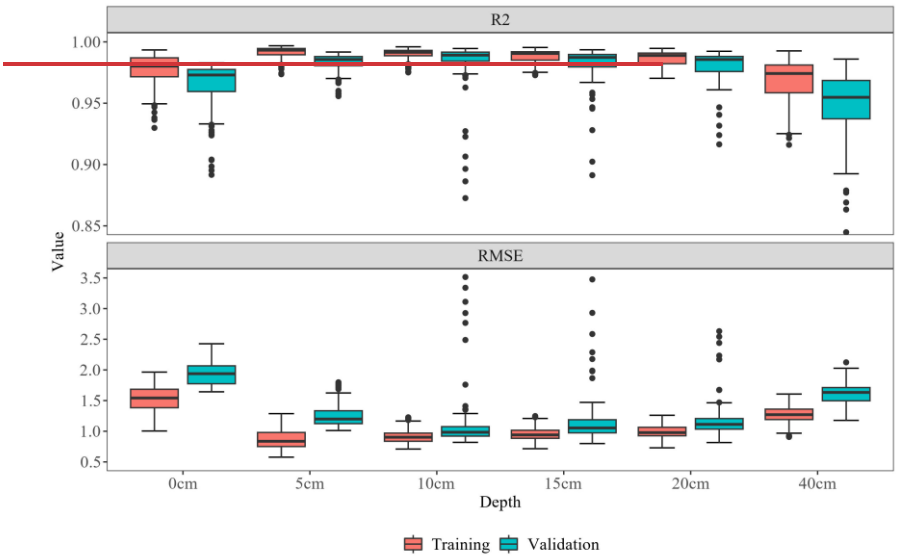

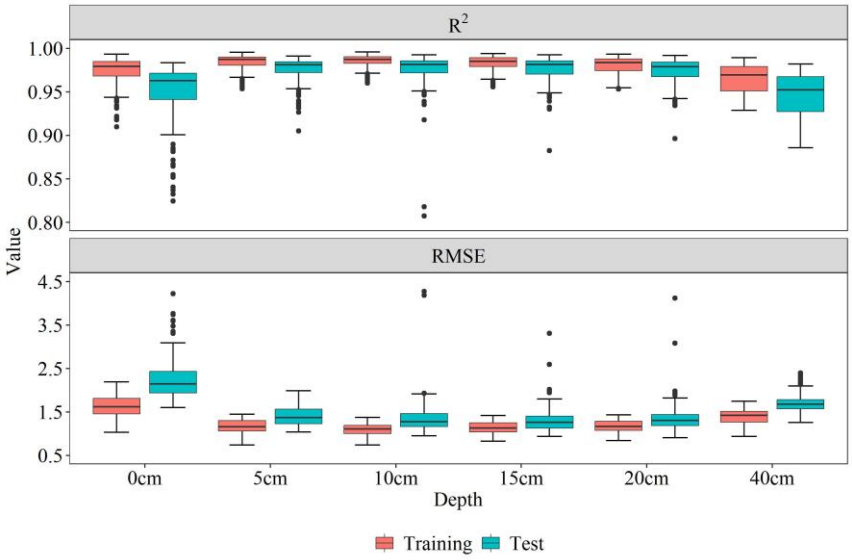

Figure 4. Model performance for training and test sets across different depths.~~Accuracy performance of model (different rotations and depths) training and validation set~~

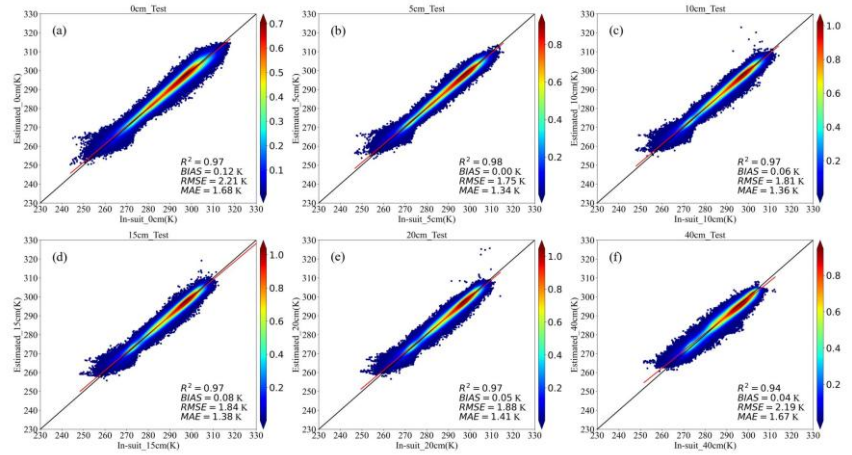

设置了格式: 字体颜色: 着色 5

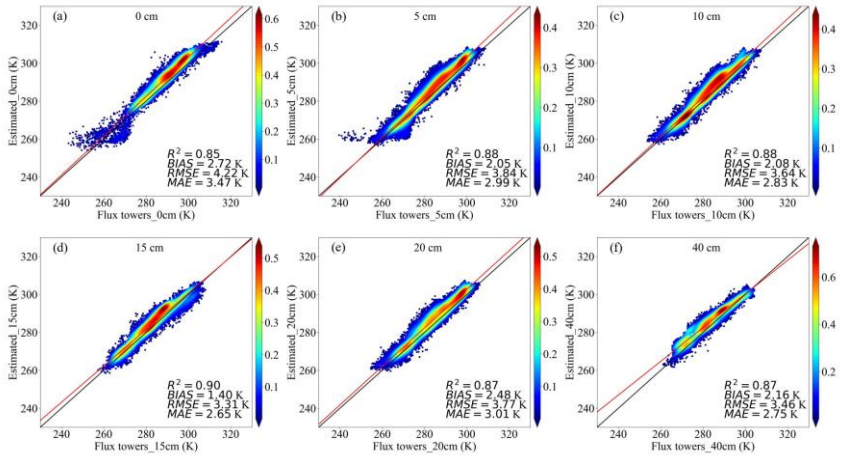

Figure 5. Density scatter plots comparing estimated daily T_s with flux tower observations at different depths~~**Figure 5.** Scatter density plot comparing the accuracy of different depths in the test set~~

设置了格式: 字体: 非加粗

带格式的: 居中

3.2 Model performance at individual sites

To evaluate spatial prediction accuracy in the spatial-scale evaluation, R^2 and RMSE were calculated at each station. Model performance was assessed across all soil depths at the station level. Spatial results show that station-level R^2 values range from 0.70 to 1.00, and RMSE values range from 0 to 3 K, indicating acceptable prediction accuracy across all soil layers. As illustrated in Figures 6 and 7, most stations achieve R^2 values above 0.90. Regions with higher prediction accuracy are mainly located in the northwest, northeast, and central areas, whereas larger errors are concentrated in the Yunnan–Guizhou Plateau (YGP) and the sparsely monitored QTP. The histogram in Fig. 7 further shows that RMSE values for most depths fall between 0.5 and 2.0 K, indicating generally good predictive performance. Notably, prediction errors were highest at the surface layer (0 cm), decreased with depth, but slightly increased again at 40 cm, where performance was weaker than at 5–20 cm~~Notably, Prediction errors at the surface layer (0 cm) are notably higher than those at greater depths. In general, error decreases with increasing depth, although a slight increase is observed at 40 cm, where performance is slightly poorer than at 5–20 cm~~.

设置了格式: 字体颜色: 蓝色

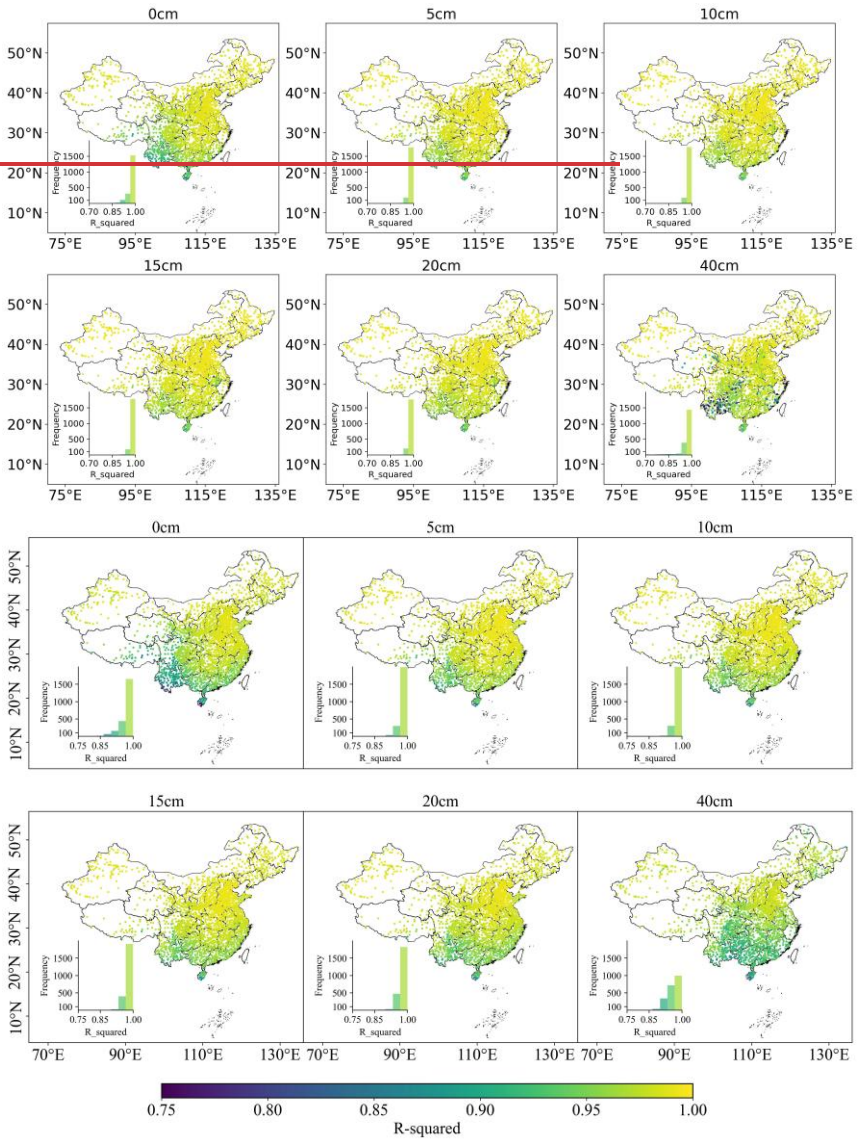

Figure 6. Goodness of R^2 across China estimated during the model testing phase. Performance metrics are calculated between predicted_T_s and in-situ T_s data sets.

设置了格式: 字体颜色: 蓝色

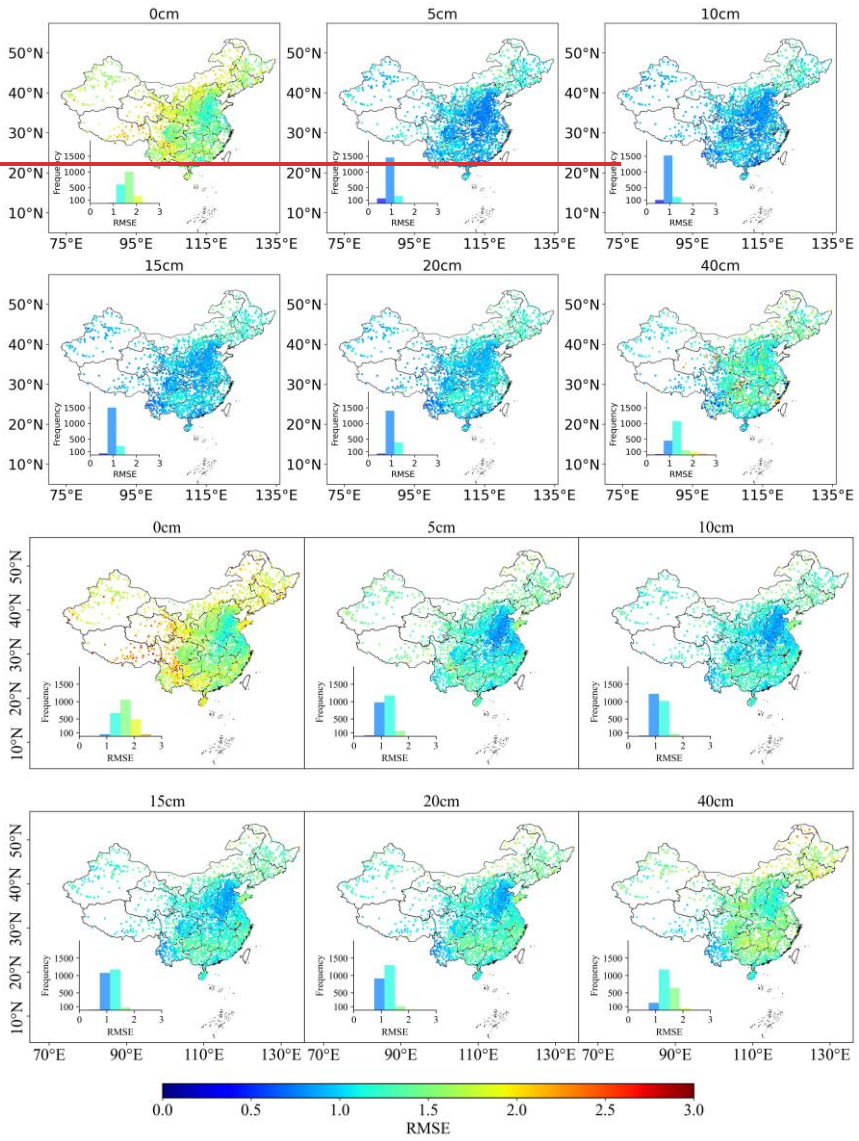

Figure 7. Goodness of RMSE across China estimated during the model testing phase. Performance metrics are calculated between predicted T_s and in-situ T_s data sets.

设置了格式: 字体颜色: 蓝色

3.3 Evaluation across land cover types and seasons

Figure 8 shows grouped box plots of the prediction performance of Ts across different land cover types (barren land, cropland, forest, and grassland) at six depths (0,

设置了格式: 字体颜色: 蓝色

5, 10, 15, 20, and 40 cm). The evaluation metrics include R^2 and RMSE. The median R^2 values across land cover types and depths range from 0.96 to 0.98, consistently exceeding 0.96 (red dashed line), indicating overall high prediction accuracy. Among land cover types, barren land exhibits the highest R^2 values, followed by cropland, while forest and grassland show slightly lower performance. The median RMSE values generally range from 1.1 to 1.8 K. Barren land shows higher RMSE compared with other land cover types, whereas cropland, forest, and grassland maintain lower and more stable RMSE. Across depths, RMSE is highest at the surface layer (0 cm), decreases steadily with increasing depth, and shows a slight increase at 40 cm~~Figure 8 shows grouped box plots illustrating the prediction performance of T_s across different land cover types (bare land, farmland, forest, grassland) at six depths (0 cm, 5 cm, 10 cm, 15 cm, 20 cm, 40 cm). The evaluation metrics include the R^2 and RMSE.~~ .

~~Mean R^2 values across all depths and land cover types range from 0.82 to 0.98, indicating overall high prediction accuracy. Notably, the mean R^2 values consistently exceed 0.96 (indicated by the red dashed line). Among the land cover categories, bare land exhibits the highest R^2 values, followed by farmland, whereas forest and grassland exhibit slightly lower performance. RMSE values vary depending on both soil depth and land cover type, generally ranging from 0.6 to 2.8 K. Bare land displays higher RMSE values, likely due to larger diurnal temperature variations and a relatively small sample size. In contrast, farmland, forest, and grassland show lower and more stable RMSE values. The highest RMSE is observed at the surface layer (0 cm), reflecting the strong sensitivity of shallow soil temperatures to external environmental conditions. RMSE tends to decrease with depth, although a slight increase is noted at 40 cm, where prediction errors are marginally higher than those at 5–20 cm.~~

Furthermore, seasonal variations in prediction accuracy are shown in Fig. 9. The median R^2 values across depths range from 0.6 to 0.98, with higher values in spring (green) and autumn (pink) and lower values in summer (orange) and winter (blue), particularly at 20–40 cm depth. The median RMSE values range from approximately 1.0 to 2.0 K, being lower in spring and autumn and higher in summer and winter, with

the largest median error observed at 40 cm depth in winter. With increasing soil depth, the median errors decrease from the surface (0 cm) to 5–10 cm, and then gradually accumulate from 15 to 40 cm~~Furthermore, seasonal variations in prediction accuracy are further presented in Fig. 9.~~.

~~The results demonstrate that the R^2 values in spring (green) and autumn (pink) are significantly higher than those in summer (orange) and winter (blue), particularly at shallow depths (0 cm and 5 cm). This suggests that the model captures T_s variability more effectively during spring and autumn. Seasonal RMSE values range approximately from 0.98 to 1.97 K, with the highest errors occurring at 0 cm depth during summer and winter. These elevated errors are likely attributed to increased surface temperature fluctuations driven by external environmental factors such as solar radiation, which add complexity to the prediction. Overall, RMSE decreases with increasing soil depth across all seasons, indicating improved thermal stability and enhanced prediction accuracy in deeper layers.~~

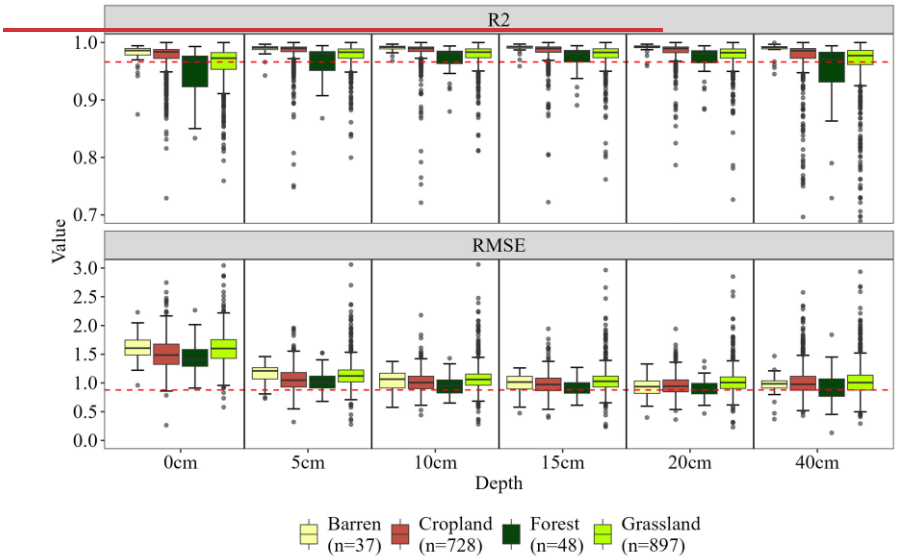

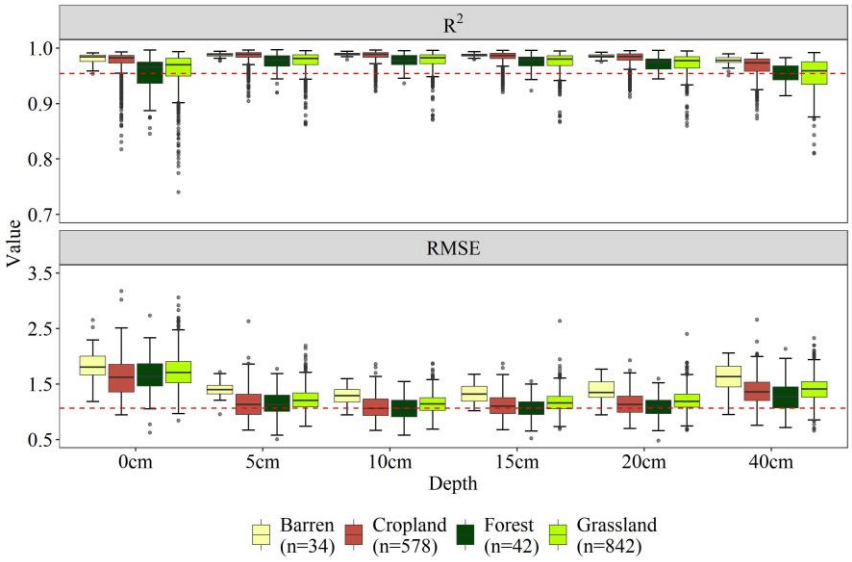

565

Figure 8. Evaluation of predicted T_s at different depths (i.e., 0, 5, 10, 15, 20, 40cm) across various land use types (i.e., Forest, Grassland, Cropland, Barren)

设置了格式: 字体颜色: 蓝色

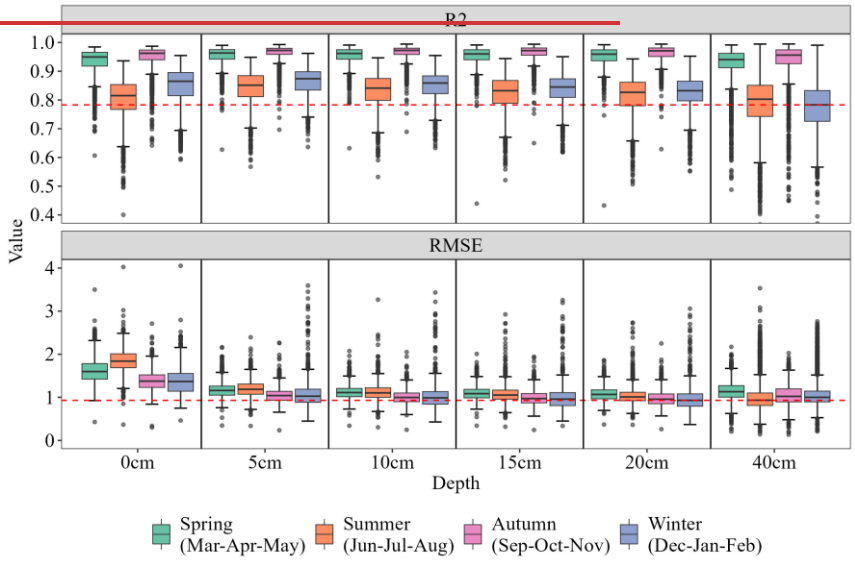

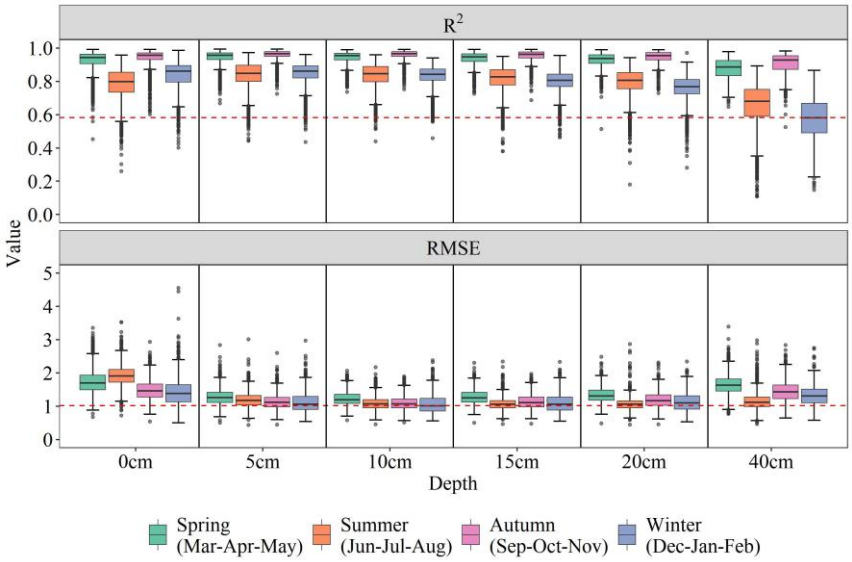

Figure 9. Evaluation of the predicted T_s in different depth (ie.0,5,10,15,20,40 cm) at sites with four seasons (i.e., spring, summer, autumn, winter). Winter is defined as December, January, and February; spring as March, April, and May; summer as June, July, and August; and autumn as September, October, and November.

设置了格式: 字体颜色: 蓝色

3.4 Comparison with other products

Figure 10 presents a comparative analysis of different T_s products at the surface (0 cm depth), evaluating the spatial characteristics of the model-generated T_s against the ERA5-Land and GLDAS 2.1 products across both national-scale regions (Fig. 10a–c) and zoomed-in local areas (Fig. 10d–f). Compared to the GLDAS 2.1 product (Fig. 11c and 11f), the model generated T_s exhibits significantly finer spatial resolution and a superior ability to capture localized spatial heterogeneity. The GLDAS 2.1 product, characterized by a coarser resolution, inadequately represents local features and exhibits notable limitations, especially in specific regions (Fig. 10f). Conversely, the spatial distribution of our T_s data closely matches that of the ERA5-Land product (Fig. 10b and 10e). Nevertheless, the ERA5-Land product may be constrained by its input resolution, whereas our adaptive modeling approach achieves greater precision in representing fine-scale spatial variability.

Scatter density plots in Fig. S5~~3~~ further indicate that our estimated T_s achieves

设置了格式: 字体颜色: 蓝色

significantly higher site-level accuracy compared to ERA5-Land and GLDAS 2.1. Specifically, the R^2 values between in-situ observations and our estimations at depths of 0, 10, and 40 cm range from 0.94 to 0.97, compared to 0.83–0.89 for ERA5-Land and 0.83–0.87 for GLDAS 2.1. These results underscore the reliability and enhanced accuracy of our T_s estimation product at both spatial and site scales, effectively overcoming the limitations associated with GLDAS 2.1 and ERA5-Land products. These findings highlight the strong potential of the model to accurately capture the spatial distribution of T_s and enhance regional-scale T_s modeling.

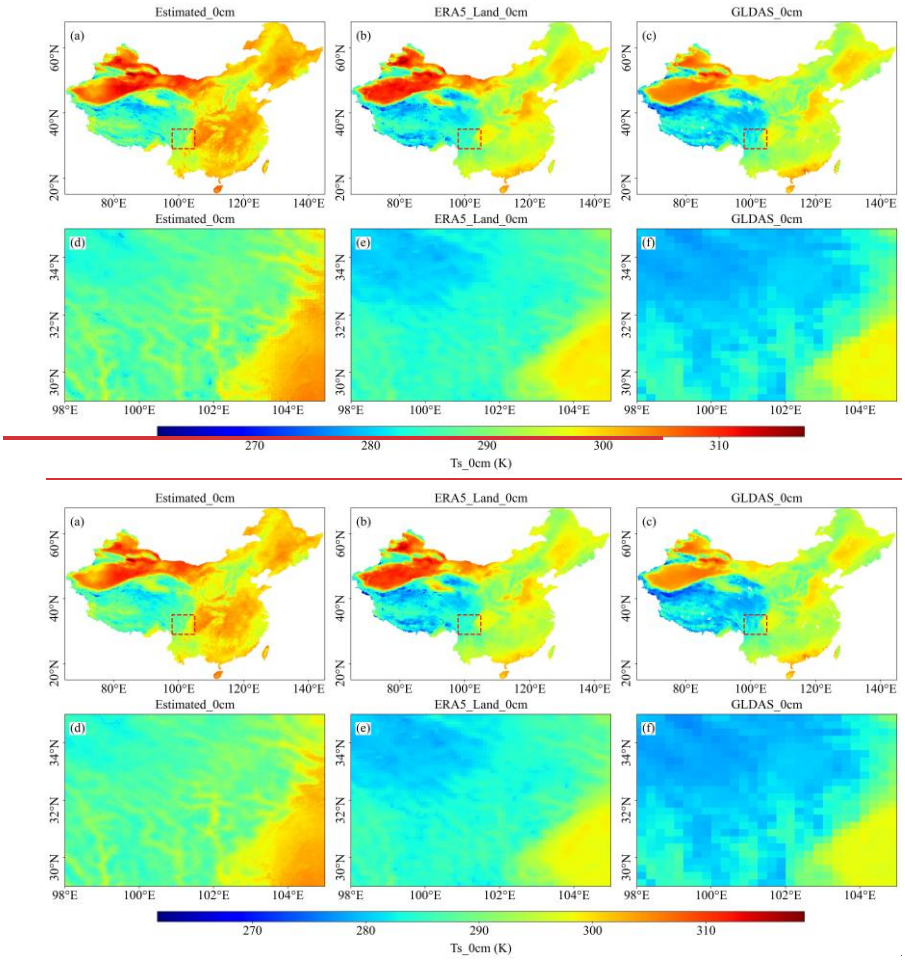

Figure 10. Comparison of different T_s products (e.g., 0 cm)

设置了格式: 字体颜色: 蓝色

3.5 Spatial and temporal patterns of T_s at varied ~~soil~~ depths across China

To examine seasonal and vertical variations in the spatial distribution of T_s, we selected two contrasting dates: January 1, 2020 (winter) and July 1, 2020 (summer). Figure 11 a–f illustrates the spatial distribution and corresponding histograms of T_s at different depths (0 cm, 5 cm, 10 cm, 15 cm, 20 cm, 40 cm) across China on January 1, 2020. The results show that T_s in northern China (particularly in the northeast, northwest, and the QTP) is generally lower in January, exhibiting distinct cold zones. In contrast, southern areas exhibit higher T_s values, forming a gradual north-to-south temperature gradient. Moreover, deeper soil layers (e.g., 40 cm) exhibit higher temperatures than surface layers (0 cm), especially in northeastern China and the QTP, reflecting the insulating effect of deeper soils during winter.

Figure 11a1–f1 illustrates the spatial distribution and histograms of T_s on July 1, 2020. Compared to January, a significant increase in T_s is observed across China in July, with widespread high-temperature zones in the eastern and southern regions. The increase is particularly pronounced in northern areas, while changes in the south are relatively moderate. In contrast to winter conditions, T_s decreases with increasing soil depth during summer, with surface temperatures (0 cm) exceeding those at 40 cm, indicating the downward heat conduction from the surface. Overall, Comparative analysis of Fig. 11a–f and Fig. 11a1–f1 elucidates both seasonal variation and vertical patterns of T_s: deeper layers (5-40 cm) are warmer than the surface (0 cm) during winter, whereas the surface is warmer in summer. The histogram further illustrates the variation in T_s~~soil temperature~~ distribution across different depths. The results indicate that temperature fluctuations in deeper soil layers are significantly smaller than those near the surface, reflecting greater thermal stability in the subsurface. These patterns reflect the combined influences of geographic location, topography, and climatic conditions on T_s spatial distribution and vertical dynamics, offering valuable insights into soil thermal behavior.

设置了格式: 字体颜色: 蓝色

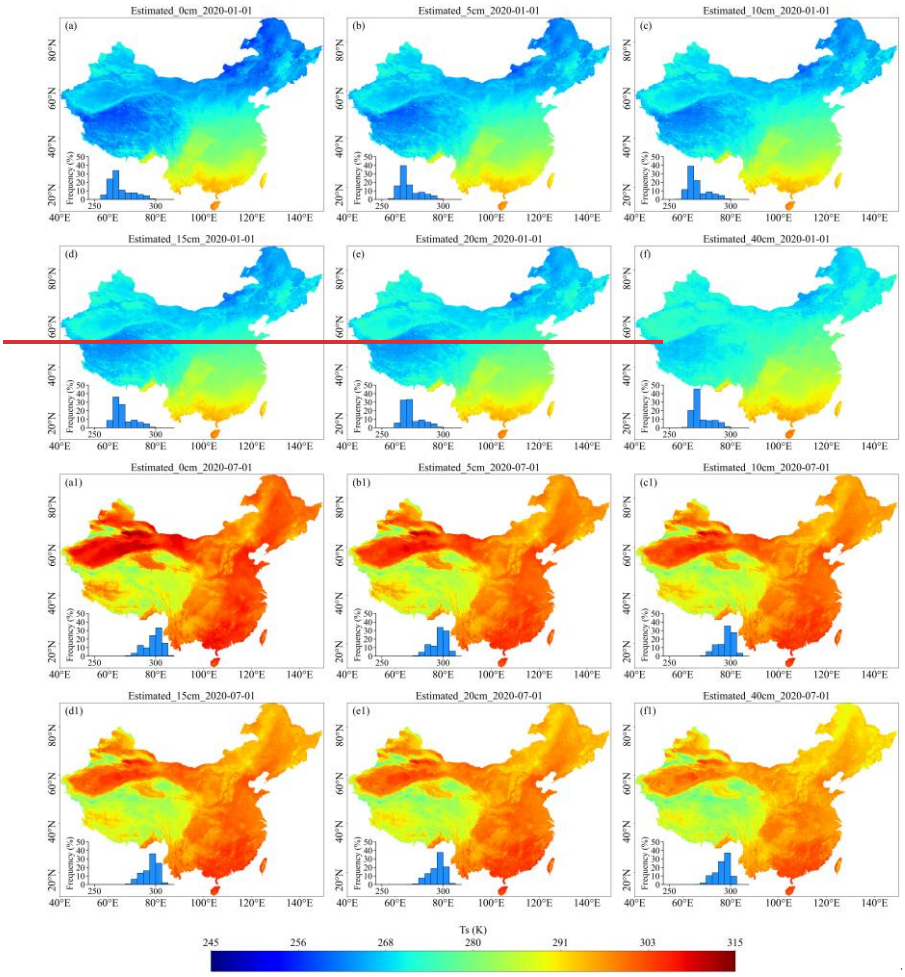
Estimated_0cm_2020-01-01
Estimated_5cm_2020-01-01
Estimated_10cm_2020-01-01
Estimated_15cm_2020-01-01
Estimated_20cm_2020-01-01
Estimated_40cm_2020-01-01
Estimated_0cm_2020-07-01
Estimated_5cm_2020-07-01
Estimated_10cm_2020-07-01
Estimated_15cm_2020-07-01
Estimated_20cm_2020-07-01
Estimated_40cm_2020-07-01
Ts (K)
245
256
268
280
291
303
315

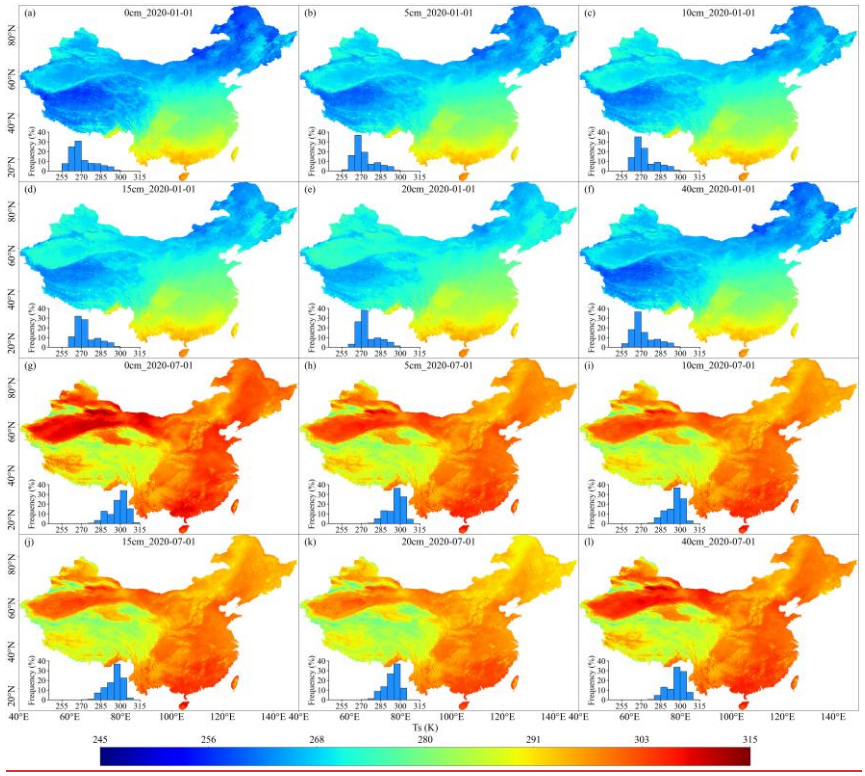

Figure 11. Spatial patterns and histograms of Estimated T_s at different depths (0, 5, 10, 15, 20, and 40 cm)

设置了格式: 字体颜色: 蓝色

To further assess the temporal performance of T_s estimation, Fig. 12 presents the time series of estimated T_s alongside in-situ measurements at four randomly selected stations (e.g., Station 56746, 99.53°E, 25.45°N) from January 2018 to January 2020. The figure displays T_s at two depths (0 cm and 40 cm), including estimated T_s (Estimated_0cm, Estimated_40cm), in-situ T_s (In-situ_0cm, In-situ_40cm), daily mean land surface temperature (Daily_mean_LST), and 2-meter air temperature (Temperature_2m). The air temperature shows distinct seasonal cycles, while T_s exhibits smoother temporal variations. In general, T_s reaches its peak during summer and its minimum in winter, though its temporal dynamics vary with soil depth. Specifically, T_s at 0 cm responds rapidly to air temperature changes and exhibits larger amplitude variations, while T_s at 40 cm shows slower responses and a noticeable lag,

reflecting the damping effect of vertical heat conduction. Site-level accuracy was evaluated using RMSE, which ranged from 0.84 K to 1.80 K across both depths, indicating strong agreement between predicted and observed values. ~~The RMSE was used to assess model accuracy, with RMSE values ranging from 1.72 K to 2.28 K for 0 cm and 40 cm depths, indicating high consistency between estimated and observed values. Notably, RMSE at the surface (0 cm) is slightly lower than at 40 cm, possibly due to stronger direct influences from surface cover and meteorological conditions.~~ Overall, the time series analysis confirms the robustness and reliability of the model in estimating T_s across varying depths, offering valuable insights into regional soil thermal dynamics.

设置了格式: 字体颜色: 蓝色

设置了格式: 字体颜色: 蓝色

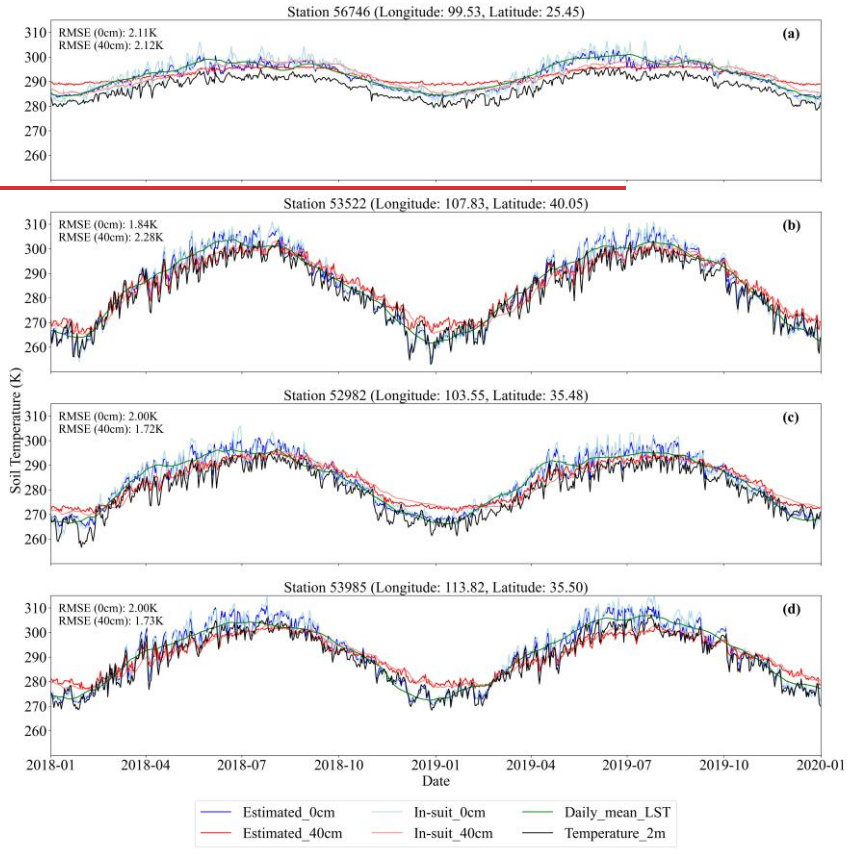

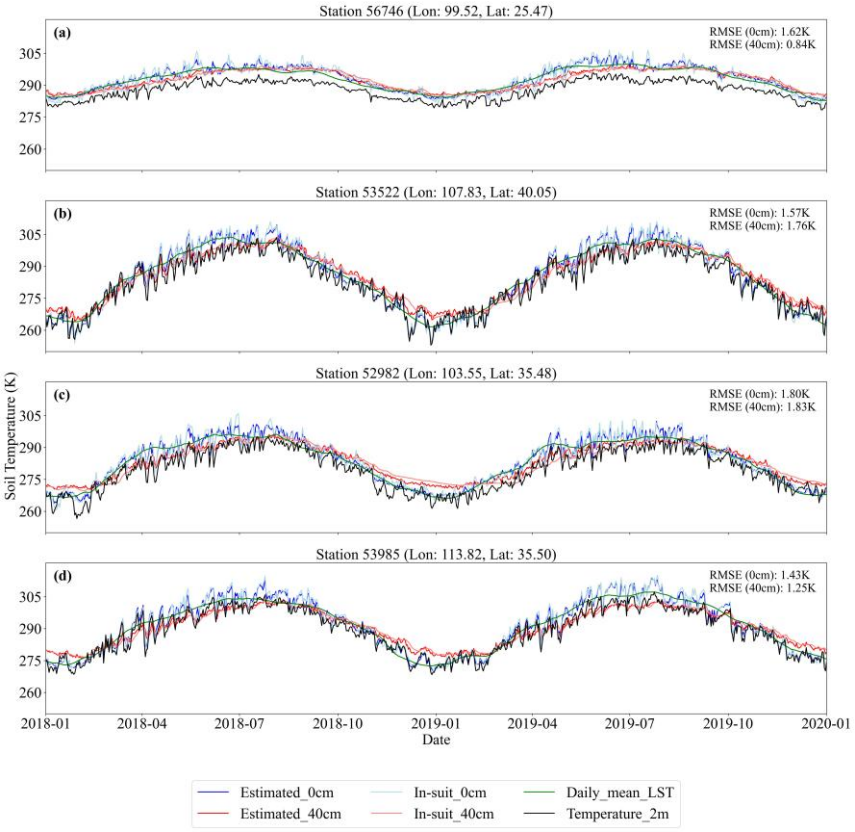

Figure 12. Time series of the Estimated_0cm, Estimated_40cm, Daily_mean_LST, and Temperature_2m at four sites from different regions between 2018-2019.

4. Discussion

4.1 The advantages of the spatially adaptive model

~~Previous studies have explored various approaches for constructing T_s datasets. For example, Lembrechts et al., (2022) constructed the Global Soil Bioclimatic Variables dataset using Random Forest models, based on time series data from 8,519 unique temperature sensors distributed across major terrestrial biomes worldwide. However, this dataset only provides long-term climatological averages. Subsequently, Wang et al., (2023) created a daily multi-layer T_s dataset for China (1980-2010) at 0.25° resolution, employing interpolation techniques including the thin-plain spline and the~~

设置了格式: 字体颜色: 着色 5

~~angular distance weight interpolation methods with over 2,000 in situ observations. However, these methods do not capture the complex nonlinear relationships between T_s and factors such as meteorology, topography, and vegetation, and its coarse spatial resolution limits detailed modeling of T_s correlations.~~

~~Reanalysis datasets, which synergize data assimilation systems with numerical weather prediction and land surface modeling frameworks, provide valuable representations of land-atmosphere interactions and subsurface heat transfer processes. These products are particularly advantageous for large-scale climate simulations and long-term environmental assessments. Yang and Zhang (2018) assessed the T_s accuracy of four reanalysis datasets (ERA-Interim/Land, MERRA-2, CFSR, and GLDAS-2.0) in China using in situ monthly mean T_s observations. The results showed that all reanalysis datasets consistently underestimated T_s across the country. More recently, the ERA5-Land and GLDAS-2.1 T_s dataset offers high temporal resolution (hourly/3-hour), but it is limited by a spatial resolution of 0.1 or 0.25 degrees. The methodological advances presented in this study address these dual challenges of accuracy and resolution. As quantified in Fig. S3, our integrated approach achieves substantial improvements in T_s estimation. Furthermore, the enhanced spatial resolution enables explicit resolution of local-scale thermal patterns that critically influence vegetation dynamics and soil biogeochemical processes.~~

~~Spatially adaptive modeling demonstrates superior adaptability and flexibility compared to traditional interpolation techniques and globally trained ML models in estimating surface T_s. A key strength of spatially adaptive approaches lies in their capacity for localized modeling, which accounts for regional variability in terrain, soil texture, and climate conditions. As illustrated in Fig. S4, the rotated-quadtree method partitions spatial grids at six different orientations, enabling it to effectively capture local spatial heterogeneity. By averaging model outputs across these rotated partitions, the approach mitigates edge effects commonly associated with static grid boundaries, resulting in smoother and more continuous spatial representations. Additionally, we examined the influence of incorporating satellite-derived LST on the model's spatial~~

~~accuracy. Figure. S5 demonstrates that LST is more effective than air temperature in detecting spatial variations in surface T_s in sparsely vegetated areas, with particularly notable improvements observed in northwestern China. This underscores the value of integrating multi-source remote sensing data, which significantly enhances the performance of spatially adaptive models, especially in areas characterized by low vegetation cover.~~

Previous studies have explored various approaches for constructing T_s datasets. For instance, Wang et al., (2023) created a daily multi-layer T_s dataset for China (1980-2010) at 0.25° resolution, employing interpolation techniques including the thin-plain spline and the angular distance weight interpolation methods with over 2,000 in-situ observations. A persistent challenge in building national-scale T_s datasets, however, lies in the highly uneven spatial distribution of observation stations—densely clustered in eastern lowlands while remaining sparse in western and high-altitude regions. Global modeling approaches, which train a single unified function across the entire domain, are inherently limited in capturing the nonlinear and non-stationary relationships between T_s and its predictors in such heterogeneous landscapes. Specifically, in sparsely sampled regions, global models lack sufficient data to learn effectively, resulting in low prediction accuracy. In contrast, in densely sampled areas, the model tends to overfit, and the training process becomes disproportionately influenced by those regions. This imbalance introduces systematic biases and limits model generalizability.

Reanalysis datasets, which synergize data assimilation systems with numerical weather prediction and land surface modeling frameworks, provide valuable representations of land-atmosphere interactions and subsurface heat transfer processes. These products are particularly advantageous for large-scale climate simulations and long-term environmental assessments. Yang and Zhang (2018) assessed the T_s accuracy of four reanalysis datasets (ERA-Interim/Land, MERRA-2, CFSR, and GLDAS-2.0) in China using in-situ monthly mean T_s observations. The results showed that all reanalysis datasets consistently underestimated T_s across the country. More recently, the ERA5-Land and GLDAS 2.1 T_s dataset offers high temporal resolution (hourly/3-hour),

带格式的: 缩进: 首行缩进: 2 字符

but it is limited by a spatial resolution of 0.1 or 0.25 degrees. Beyond reanalysis datasets, some efforts have focused on constructing empirical T_s products using ML approaches. For example, the Global Soil Bioclimatic Variables dataset (Lembrechts et al., 2022), derived from Random Forest modeling with 8,519 global sensors, provides only long-term climatological means, rather than high-resolution daily estimates.

In contrast, the methodological framework proposed in this study addresses both accuracy and resolution limitations. The spatially adaptive modeling strategy offers significant advantages over traditional interpolation and globally trained ML models. Its core strength lies in localized modeling, which accounts for regional variability in topography, soil properties, and climate conditions. As shown in Fig. S6, the rotated quadtree strategy partitions space at six orientations (0°–75°), enabling a more nuanced representation of spatial heterogeneity. By averaging predictions across these rotated configurations, the method reduces boundary artifacts often associated with static grids, resulting in smoother and more continuous spatial outputs. Moreover, the fine spatial resolution (1 km) enables the model to resolve localized thermal patterns that are critical for understanding vegetation dynamics and soil biogeochemistry. We also assessed the contribution of satellite-derived LST to model performance. As shown in Figs. S7 and S8, incorporating LST as an input variable, relative to using only air temperature, significantly enhances overall modeling accuracy and improves performance across sites with different land cover types, with the most pronounced improvements observed in barren land areas. This highlights the importance of multi-source data fusion in boosting the performance of spatially adaptive models under data-scarce conditions. In summary, our spatially adaptive local modeling approach offers a more robust and scalable solution for large-scale T_s estimation under heterogeneous station distributions and complex environmental conditions.

带格式的: 缩进: 首行缩进: 2 字符

设置了格式: 字体颜色: 着色 5

设置了格式: 字体颜色: 蓝色

设置了格式: 非突出显示

设置了格式: 字体颜色: 蓝色

设置了格式: 字体颜色: 着色 5

4.2 Potential applications of the T_s product

The high-resolution, multi-layer T_s datasets generated using the spatially adaptive estimation method fill a significant data gap in China, where comprehensive T_s profile

records are scarce. As a key biophysical variable, T_s provides crucial insights into soil–atmosphere interactions that are not captured by air temperature alone. In agricultural systems, T_s governs fundamental processes throughout the crop life cycle—from sowing and germination to growth and yield formation (Rahman et al., 2019). Multi-layer T_s data can optimize accumulated temperature models, enhancing the precision of sowing decisions and supporting sustainable field management. Additionally, T_s influences nutrient decomposition and water movement within soil profiles (Jebamalar et al., 2012), directly impacting soil fertility, moisture retention, and thus, the overall efficiency of agroecosystems.

Beyond agricultural applications, T_s is increasingly recognized as a critical variable for assessing ecosystem responses to climate extremes. For instance, Fan et al., (2024) proposed the Soil Composite Drought Heatwave ~~Soil Composite Drought Heatwave (SCDHW)~~ index to evaluate the severity of concurrent drought and heatwave events. However, their findings show that existing reanalysis datasets often underestimate these events compared to observational records, highlighting the need for more accurate, high-resolution T_s data. In the context of intensifying global warming and extreme climate events, access to reliable T_s datasets is essential for improving the monitoring and prediction of environmental stressors. These advancements are not only vital for understanding terrestrial ecosystem dynamics but also for strengthening climate resilience at both regional and national scales.

Moreover, T_s plays a pivotal role in ecological and hydrological modeling, offering a more direct representation of surface processes than air temperature. It serves as a sensitive indicator of biogeochemical cycles and phenological changes (Lembrechts et al., 2022). For example, Liu et al., (2024) demonstrated that T_s is a dominant driver of spring phenology in Chinese forests, making it a valuable input for climate–vegetation interaction models. In cold regions, T_s governs soil freeze–thaw cycles, which are critical for hydrological processes such as runoff generation, groundwater recharge, and permafrost monitoring (Smith et al., 2022; Xu et al., 2022). Furthermore, T_s is a key driver of soil respiration, influencing CO_2 fluxes and terrestrial carbon cycling (Lloyd

设置了格式: 字体颜色: 蓝色

设置了格式: 非突出显示

and Taylor, 1994; Hursh et al., 2017). As such, the development of high-resolution T_s products enables more accurate simulation of ecosystem carbon dynamics and regional carbon budgeting, thereby advancing our understanding of climate feedback mechanisms.

4.3 Limitations and future perspective

Despite the strong performance of our spatially adaptive T_s estimation framework, several limitations warrant acknowledgment. As shown in Figures 6 and 7, model validation at station level reveals spatial heterogeneity in prediction accuracy, with relatively lower performance observed in the YGP and the QTP regions. On the one hand, as evidenced by Figure 10, our multi-source modeling framework captures T_s variations across different elevations and geomorphic conditions more effectively than existing datasets. However, the QTP and YGP are characterized by complex terrain and high altitudes, coupled with rapidly changing climatic conditions, which significantly complicate T_s estimation. These findings align with previous studies showing that high elevations intensify the disconnect between air temperature and LST, thereby increasing the uncertainty in thermal modeling (Mo et al., 2025).

MODIS LST serves as a critical input to our modeling framework. However, as an optical remote sensing product, it is highly susceptible to cloud contamination, often resulting in data gaps. Despite the use of spatiotemporal interpolation and SG filtering, residual uncertainties persist in the reconstructed LST data. Future improvements in T_s reconstruction can be pursued along two main directions. First, more physically grounded LST reconstruction methods can be adopted, such as incorporating surface energy balance models and diurnal temperature cycle models (Hong et al., 2022; Firozjaei et al., 2024; Wang et al., 2024). These methods apply energy conservation principles to estimate T_s during periods of missing or unreliable observations, thereby providing more realistic estimates of land surface thermal conditions during periods of cloud cover. Second, integrating higher temporal resolution remote sensing observations may help overcome the limitations of MODIS. For instance, passive

带格式的: 缩进: 首行缩进: 2 字符

设置了格式: 字体: (中文) 宋体, 字体颜色: 着色 5

设置了格式: 字体: (中文) 宋体

设置了格式: 字体: (中文) 宋体, 字体颜色: 着色 5

设置了格式: 字体颜色: 着色 5

microwave satellite data provide all-weather observations and are less sensitive to cloud interference (Duan et al., 2017; Wu et al., 2022). In addition, next-generation geostationary satellites such as Himawari-8 offer observations at 10-minute intervals, substantially enhancing the temporal continuity and quality of surface temperature estimates (Yamamoto et al., 2022; You et al., 2024). These enhancements are expected to significantly improve the accuracy and temporal continuity of soil temperature monitoring.

Our results (Figures 8 and 9) show that model accuracy varies across different soil depths, with additional influences from season and land use. Accuracy is relatively lower at the surface (0 cm), improves at intermediate depths (5–10 cm), and then declines again at greater depths (20–40 cm). This depth-dependent pattern can be explained by the physical characteristics of soil temperature. Surface soil temperature is highly sensitive to short-term meteorological fluctuations such as radiation, precipitation, and evapotranspiration, leading to greater spatiotemporal variability and larger prediction errors. In contrast, intermediate soil layers benefit from the buffering effects of thermal diffusion and soil heat capacity, which dampen high-frequency fluctuations and stabilize the relationship between predictors and T_s, thereby improving performance at these depths. At greater depths, however, surface-level errors propagate downward through the cascading framework, resulting in reduced accuracy — particularly during summer and winter.

~~(Prigent et al., 2016)~~(Prigent et al., 2016)~~(Yamamoto et al., 2022; You et al., 2024)~~Seasonal changes and variations in land cover further contribute to differences in estimation accuracy. As shown in Figures 8 and 9, the model exhibits higher accuracy in spring and autumn, whereas its performance tends to decline during summer and winter. During summer, dense vegetation growth and canopy closure reduce the influence of surface–atmosphere energy exchanges on T_s, weakening the correlation between canopy temperature and subsurface T_s (Kropp et al., 2020; Cui et al., 2022). In winter, snow cover introduces a suite of confounding effects: high surface albedo

设置了格式: 字体颜色: 着色 5

设置了格式: 字体颜色: 着色 5

设置了格式: 字体颜色: 着色 5

设置了格式: 字体颜色: 着色 5

reduces net radiation (Loranty et al., 2014; Li et al., 2018), while snow acts as an insulator, limiting the soil's response to cold air incursions (Zhang, 2005; Myers-Smith et al., 2015). Additionally, low temperatures lead to soil water freezing, which alters the soil's thermal conductivity and heat storage capacity. These factors, together with frequent freeze–thaw cycles, introduce complex nonlinear dynamics in T_s that increase modeling uncertainty (Li et al., 2023a; Imanian et al., 2024). While our multi-source adaptive modeling framework performs well across depths, it does not explicitly account for the physical mechanisms of vertical heat transfer. Future research could explore deep learning models that are capable of learning complex spatiotemporal features and improving the physical interpretability of T_s variations across time, space, and depth.

~~Despite the promising performance of our spatially adaptive T_s estimation framework, several limitations should be acknowledged. As illustrated in Fig. 7, stations with relatively low estimation accuracy are primarily located in southwestern China. One key factor is the reliance on MODIS data from polar-orbiting satellites, which have low temporal resolution (1–16 days) and provide instantaneous snapshots rather than continuous observations. Although we employed a spatiotemporal linear interpolation method to reconstruct missing data caused by cloud contamination, residual uncertainties remain inevitable. In high-altitude regions such as the QTP and the YGP, complex topography and rapidly changing climatic conditions further exacerbate the difficulty of accurate T_s prediction, consistent with findings reported by Mo et al., (2025).~~

~~Seasonal dynamics and land cover types also introduce considerable variability in estimation performance. The model generally performs better in spring and autumn, while summer and winter present greater challenges. During summer, dense vegetation growth and canopy closure reduce the influence of surface–atmosphere energy exchanges on T_s, weakening the correlation between canopy temperature and subsurface soil temperature (Kropp et al., 2020; Cui et al., 2022). In winter, snow cover introduces a suite of confounding effects: high surface albedo reduces net radiation~~

设置了格式: 字体颜色: 着色 5

设置了格式: 字体颜色: 着色 5

设置了格式: 突出显示

~~(Loranty et al., 2014; Li et al., 2018), while snow acts as an insulator, limiting the soil's response to cold air incursions (Zhang, 2005; Myers-Smith et al., 2015). Additionally, low temperatures lead to soil water freezing, altering thermal conductivity and heat capacity. These changes, along with repeated freeze–thaw cycles, introduce significant nonlinearity and temporal variability in T_s, ultimately reducing model accuracy (Li et al., 2023a; Imanian et al., 2024).~~

~~Future studies could address these limitations by incorporating data from microwave satellite sensors, which offer all-weather imaging capabilities and can reduce information loss caused by cloud cover in optical sensors like MODIS (Prigent et al., 2016). Moreover, leveraging data from next-generation geostationary satellites (e.g., Himawari-8), which provide observations at 10-minute intervals, may significantly enhance temporal continuity and quality (Yamamoto et al., 2022; You et al., 2024). Combining high-frequency geostationary data with traditional optical sources holds great potential for advancing T_s monitoring. While our multi-source data-driven ML model has shown strong predictive capability across multiple depths, current variable importance analyses lack a mechanistic explanation for vertical heat conduction processes. Future research could explore deep learning models that are capable of learning complex spatiotemporal features and improving the physical interpretability of T_s variations across time, space, and depth.~~

5. Conclusion

This study addresses the lack of high spatiotemporal resolution multi-layer T_s data by proposing a spatially adaptive ML framework, successfully constructing a retrieval model for multi-layer T_s. By integrating in-situ observations, reanalysis data, satellite remote sensing data, as well as topographic and soil texture data, the model demonstrates high accuracy across different depths, seasons, and land use types. ~~Independent validation results indicate that the model performs better in springs and autumns compared to summers and winters, and shows superior performance in bare land, cropland, and grassland compared to forest.~~ The results indicate relatively higher

设置了格式: 字体颜色: 蓝色

performance in spring and autumn than in summer and winter, and greater accuracy in bare land, cropland, and grassland compared with forested areas. In comparison with ERA5-Land and GLDAS 2.1 T_s products, the multi-layer T_s data generated in this study exhibit significant improvements in both accuracy and spatial detail~~Compared to ERA5_Land and GLDAS 2.1 T_s, the multi-layer T_s data generated in this study exhibits significant advantages in both accuracy and spatial detail~~. Based on this framework~~Based on this model~~, we have first developed the long-term (2010-2020) high spatiotemporal resolution (daily, 1 km resolution) multi-layer (0, 5, 10, 15, 20, 40 cm) T_s dataset for China. Future research could further explore methods that simultaneously integrate temporal, spatial, and depth information, and utilize multi-source sensor data to enhance the spatiotemporal monitoring capabilities of T_s at different depths. Overall, this study demonstrates the potential of multi-source data in T_s estimation and provides a reliable tool and data foundation for ecological modeling, agricultural production and related studies.

设置了格式: 字体颜色: 蓝色
设置了格式: 字体颜色: 蓝色
设置了格式: 字体颜色: 蓝色
设置了格式: 字体颜色: 蓝色

6. Data availability

The daily multi-layer T_s products (0, 5, 10, 15, 20, and 40 cm) at 1 km resolution from 2010 to 2020 are freely available in HDF5 format to the public at https://doi.org/10.11888/Terre.tpdc.302333 (Wang et al., 2025b). In addition, monthly multi-layer T_s data are also provided to meet the needs of various users.

带格式的: 缩进: 首行缩进: 2 字符

Author contributions. XW, JM and HS developed the methodology and designed the experiments. LH and XW collected and processed the data. XW wrote the first draft of the paper under the supervision of other authors. All authors participated in the review and editing of the paper.

Competing interests. Author Hao Shi is a member of the editorial board of Earth System Science Data. The contact author has declared that no other competing interests

are present.

Acknowledgments. We gratefully acknowledge the National Meteorological Center of the China Meteorological Administration for providing the observed T_s data. We thank the NASA Earth Observing System Data and Information System for providing MODIS and DEM data, and the European Centre for Medium-Range Weather Forecasts for the ERA5-Land reanalysis dataset. We also acknowledge the Soil SubCenter of the National Earth System Science Data Center, National Science & Technology Infrastructure of China (http://soil.geodata.cn), for providing soil texture data. The flux tower data used for independent validation were provided by the ChinaFLUX network through the National Ecosystem Science Data Center, National Science & Technology Infrastructure of China (http://www.nesdc.org.cn).~~We gratefully acknowledge the National Meteorological Center of the China Meteorological Administration for providing the observed T_s data. We thank the NASA Earth Observing System Data and Information System for providing MODIS and DEM data, and the European Centre for Medium-Range Weather Forecasts for the ERA5-Land reanalysis dataset. We also acknowledge the Soil SubCenter of the National Earth System Science Data Center, National Science & Technology Infrastructure of China (http://soil.geodata.cn), for providing soil texture data.~~

Financial support. This work was supported by the National Key Research and Development Program of China (Grant No. 2023YFF1303700) and the National Natural Science Foundation of China (No. 42375195).

设置了格式: 字体: 非加粗, 字体颜色: 蓝色

设置了格式: 字体颜色: 蓝色

设置了格式: 字体: 非加粗, 字体颜色: 蓝色

带格式的: 行距: 单倍行距

带格式的: 无

Reference

Akinwande, M. O., Dikko, H. G., and Samson, A.: Variance inflation factor: As a condition for the inclusion of suppressor variable(s) in regression analysis, Open J. Stat., 5, 754–767, https://doi.org/10.4236/ojs.2015.57075, 2015.

Badache, M., Eslami-Nejad, P., Ouzzane, M., Aidoun, Z., and Lamarche, L.: A new modeling approach for improved ground temperature profile determination, Renew. Energy, 85, 436–444, https://doi.org/10.1016/j.renene.2015.06.020, 2016.

Bayatvarkeshi, M., Bhagat, S. K., Mohammadi, K., Kisi, O., Farahani, M., Hasani, A., Deo, R., and Yaseen, Z. M.: Modeling soil temperature using air temperature features in diverse climatic conditions with complementary machine learning models, Comput. Electron. Agric., 185, 106158, https://doi.org/10.1016/j.compag.2021.106158, 2021.

Bond-Lamberty, B., Wang, C., and Gower, S. T.: Spatiotemporal measurement and modeling of stand-level boreal forest soil temperatures, Agric. For. Meteorol., 131, 27–40, https://doi.org/10.1016/j.agrformet.2005.04.008, 2005.

Bright, R. M., Davin, E., O'Halloran, T., Pongratz, J., Zhao, K., and Cescatti, A.: Local temperature response to land cover and management change driven by non-radiative processes, Nat. Clim. Change, 7, 296 – 302, https://doi.org/10.1038/NCLIMATE3250, 2017.

Cao, R., Chen, Y., Shen, M., Chen, J., Zhou, J., Wang, C., and Yang, W.: A simple method to improve the quality of NDVI time-series data by integrating spatiotemporal information with the Savitzky-Golay filter, Remote Sens. Environ., 217, 244–257, https://doi.org/10.1016/j.rse.2018.08.022, 2018.

Chen, L., Aalto, J., and Luoto, M.: Observed Decrease in Soil and Atmosphere

带格式的: 无

设置了格式: 字体: (默认) Times New Roman, 小四

带格式的: 缩进: 左侧: 0 厘米, 悬挂缩进: 2 字符, 首行缩进: -2 字符

Temperature Coupling in Recent Decades Over Northern Eurasia, Geophys. Res. Lett., 48, e2021GL092500, https://doi.org/10.1029/2021GL092500, 2021a.

Chen, T. and Guestrin, C.: Xgboost: A scalable tree boosting system, in: Proceedings of the 22nd acm sigkdd international conference on knowledge discovery and data mining, 785–794, https://doi.org/10.1145/2939672.2939785, 2016.

Chen, X., Long, D., Hong, Y., Zeng, C., and Yan, D.: Improved modeling of snow and glacier melting by a progressive two-stage calibration strategy with GRACE and multisource data: How snow and glacier meltwater contributes to the runoff of the U pper B rahmaputra R iver basin?, Water Resour. Res., 53, 2431 – 2466, https://doi.org/10.1002/2016WR019656, 2017.

Chen, Y., Cao, R., Chen, J., Liu, L., and Matsushita, B.: A practical approach to reconstruct high-quality Landsat NDVI time-series data by gap filling and the Savitzky – Golay filter, ISPRS J. Photogramm. Remote Sens., 180, 174 – 190, https://doi.org/10.1016/j.isprsjprs.2021.08.015, 2021b.

Cui, X., Xu, G., He, X., and Luo, D.: Influences of seasonal soil moisture and temperature on vegetation phenology in the Qilian Mountains, Remote Sens., 14, 3645, https://doi.org/10.3390/rs14153645, 2022.

Duan, S.-B., Li, Z.-L., and Leng, P.: A framework for the retrieval of all-weather land surface temperature at a high spatial resolution from polar-orbiting thermal infrared and passive microwave data, Remote Sens. Environ., 195, 107 – 117, https://doi.org/10.1016/j.rse.2017.04.008, 2017.

Fan, X., Zhang, Y., Shi, K., Peng, J., Liu, Y., Zhou, Y., Liu, Y., Zhu, Q., Song, C., Wan, R., Zhao, X., and Woolway, R. I.: Surging compound drought – heatwaves underrated in global soils, Proc. Natl. Acad. Sci., 121, e2410294121, https://doi.org/10.1073/pnas.2410294121, 2024.

Farhangmehr, V., Imanian, H., Mohammadian, A., Cobo, J. H., Shirkhani, H., and Payeur, P.: A spatiotemporal CNN-LSTM deep learning model for predicting soil temperature in diverse large-scale regional climates, Sci. Total Environ., 968, 178901, https://doi.org/10.1016/j.scitotenv.2025.178901, 2025.

Farr, T. G., Rosen, P. A., Caro, E., Crippen, R., Duren, R., Hensley, S., Kobrick, M., Paller, M., Rodriguez, E., Roth, L., Seal, D., Shaffer, S., Shimada, J., Umland, J., Werner, M., Oskin, M., Burbank, D., and Alsdorf, D.: The Shuttle Radar Topography Mission, Rev. Geophys., 45, https://doi.org/10.1029/2005RG000183,

2007.

Feng, Y., Cui, N., Hao, W., Gao, L., and Gong, D.: Estimation of soil temperature from meteorological data using different machine learning models, Geoderma, 338, 67–77, https://doi.org/10.1016/j.geoderma.2018.11.044, 2019.

Firozjaei, M. K., Mijani, N., Kiavarz, M., Duan, S.-B., Atkinson, P. M., and Alavipanah, S. K.: A novel surface energy balance-based approach to land surface temperature downscaling, Remote Sens. Environ., 305, 114087, https://doi.org/10.1016/j.rse.2024.114087, 2024.

Gao, Z., Lenschow, D. H., Horton, R., Zhou, M., Wang, L., and Wen, J.: Comparison of two soil temperature algorithms for a bare ground site on the Loess Plateau in China, J. Geophys. Res. Atmospheres, 113, https://doi.org/10.1029/2008JD010285, 2008.

Hong, F., Zhan, W., Göttsche, F.-M., Liu, Z., Dong, P., Fu, H., Huang, F., and Zhang, X.: A global dataset of spatiotemporally seamless daily mean land surface temperatures: Generation, validation, and analysis, Earth Syst. Sci. Data, 14, 3091–3113, https://doi.org/10.5194/essd-14-3091-2022, 2022.

Hu, G., Zhao, L., Wu, X., Li, R., Wu, T., Xie, C., Qiao, Y., Shi, J., Li, W., and Cheng, G.: New Fourier-series-based analytical solution to the conduction–convection equation to calculate soil temperature, determine soil thermal properties, or estimate water flux, Int. J. Heat Mass Transf., 95, 815 – 823, https://doi.org/10.1016/j.ijheatmasstransfer.2015.11.078, 2016.

Huang, R., Huang, J., Zhang, C., Ma, H., Zhuo, W., Chen, Y., Zhu, D., Wu, Q., and Mansaray, L. R.: Soil temperature estimation at different depths, using remotely-sensed data, J. Integr. Agric., 19, 277 – 290, https://doi.org/10.1016/S2095-3119(19)62657-2, 2020.

Huete, A., Didan, K., Miura, T., Rodriguez, E. P., Gao, X., and Ferreira, L. G.: Overview of the radiometric and biophysical performance of the MODIS vegetation indices, Remote Sens. Environ., 83, 195 – 213, https://doi.org/10.1016/S0034-4257(02)00096-2, 2002.

Hursh, A., Ballantyne, A., Cooper, L., Maneta, M., Kimball, J., and Watts, J.: The sensitivity of soil respiration to soil temperature, moisture, and carbon supply at

the global scale, Glob. Change Biol., 23, 2090 – 2103, https://doi.org/10.1111/gcb.13489, 2017.

Imanian, H., Mohammadian, A., Farhangmehr, V., Payeur, P., Goodarzi, D., Hiedra Cobo, J., and Shirkhani, H.: A comparative analysis of deep learning models for soil temperature prediction in cold climates, Theor. Appl. Climatol., 155, 2571–2587, https://doi.org/10.1007/s00704-023-04781-x, 2024.

Jebamalar, A. S., Raja, S., and Bai, S.: Prediction of annual and seasonal soil temperature variation using artificial neural network, 9240 Lg 8435 I, 2012.

Karthikeyan, L. and Mishra, A. K.: Multi-layer high-resolution soil moisture estimation using machine learning over the United States, Remote Sens. Environ., 266, 112706, https://doi.org/10.1016/j.rse.2021.112706, 2021.

Khosravi, K., Golkarian, A., Barzegar, R., Aalami, M. T., Heddam, S., Omidvar, E., Keesstra, S. D., and L ó pez-vicente, M.: Multi-step ahead soil temperature forecasting at different depths based on meteorological data: Integrating resampling algorithms and machine learning models, Pedosphere, 33, 479–495, https://doi.org/10.1016/j.pedsph.2022.06.056, 2023.

Kong, D., Zhang, Y., Gu, X., and Wang, D.: A robust method for reconstructing global MODIS EVI time series on the Google Earth Engine, ISPRS J. Photogramm. Remote Sens., 155, 13–24, https://doi.org/10.1016/j.isprsjprs.2019.06.014, 2019.

Kropp, H., Loranty, M. M., Natali, S. M., Kholodov, A. L., Rocha, A. V., Myers-Smith, I., Abbot, B. W., Abermann, J., Blanc-Betes, E., Blok, D., Blume-Werry, G., Boike, J., Breen, A. L., Cahoon, S. M. P., Christiansen, C. T., Douglas, T. A., Epstein, H. E., Frost, G. V., Goeckede, M., Høye, T. T., Mamet, S. D., O'Donnell, J. A., Olefeldt, D., Phoenix, G. K., Salmon, V. G., Sannel, A. B. K., Smith, S. L., Sonnentag, O., Vaughn, L. S., Williams, M., Elberling, B., Gough, L., Hjort, J., Lafleur, P. M., Euskirchen, E. S., Heijmans, M. M., Humphreys, E. R., Iwata, H., Jones, B. M., Jorgenson, M. T., Grünberg, I., Kim, Y., Laundre, J., Mauritz, M., Michelsen, A., Schaepman-Strub, G., Tape, K. D., Ueyama, M., Lee, B.-Y., Langley, K., and Lund, M.: Shallow soils are warmer under trees and tall shrubs across arctic and boreal ecosystems, Environ. Res. Lett., 16, 015001, https://doi.org/10.1088/1748-9326/abc994, 2020.

Lembrechts, J. J., van den Hoogen, J., Aalto, J., Ashcroft, M. B., De Frenne, P.,

Kemppinen, J., Kopecký, M., Luoto, M., Maclean, I. M. D., Crowther, T. W., Bailey, J. J., Haesen, S., Klinges, D. H., Niittynen, P., Scheffers, B. R., Van Meerbeek, K., Aartsma, P., Abdalaze, O., Abedi, M., Aerts, R., Ahmadian, N., Ahrends, A., Alatalo, J. M., Alexander, J. M., Allonsius, C. N., Altman, J., Ammann, C., Andres, C., Andrews, C., Ardö, J., Arriga, N., Arzac, A., Aschero, V., Assis, R. L., Assmann, J. J., Bader, M. Y., Bahalkeh, K., Barančok, P., Barrio, I. C., Barros, A., Barthel, M., Basham, E. W., Bauters, M., Bazzichetto, M., Marchesini, L. B., Bell, M. C., Benavides, J. C., Benito Alonso, J. L., Berauer, B. J., Bjerke, J. W., Björk, R. G., Björkman, M. P., Björnsdóttir, K., Blonder, B., Boeckx, P., Boike, J., Bokhorst, S., Brum, B. N. S., Brůna, J., Buchmann, N., Buysse, P., Camargo, J. L., Campoe, O. C., Candan, O., Canessa, R., Cannone, N., Carbognani, M., Carnicer, J., Casanova-Katny, A., Cesarz, S., Chojnicki, B., Choler, P., Chown, S. L., Cifuentes, E. F., Čiliak, M., Contador, T., Convey, P., Cooper, E. J., Cremonese, E., Curasi, S. R., Curtis, R., Cutini, M., Dahlberg, C. J., Daskalova, G. N., de Pablo, M. A., Della Chiesa, S., Dengler, J., Deronde, B., Descombes, P., Di Cecco, V., Di Musciano, M., Dick, J., Dimarco, R. D., Dolezal, J., Dorrepaal, E., Dušek, J., Eisenhauer, N., Eklundh, L., Erickson, T. E., et al.: Global maps of soil temperature, Glob. Change Biol., 28, 3110 – 3144, https://doi.org/10.1111/gcb.16060, 2022.

Li, B., Liang, S., Ma, H., Dong, G., Liu, X., He, T., and Zhang, Y.: Generation of global 1 km all-weather instantaneous and daily mean land surface temperatures from MODIS data, Earth Syst. Sci. Data, 16, 3795 – 3819, https://doi.org/10.5194/essd-16-3795-2024, 2024a.

Li, N., Wang, L., and Chen, D.: Vegetation greening amplifies shallow soil temperature warming on the Tibetan Plateau, Npj Clim. Atmospheric Sci., 7, 1 – 12, https://doi.org/10.1038/s41612-024-00651-z, 2024b.

Li, Q., Ma, M., Wu, X., and Yang, H.: Snow cover and vegetation-induced decrease in global albedo from 2002 to 2016, J. Geophys. Res. Atmospheres, 123, 124–138, https://doi.org/10.1002/2017JD027010, 2018.

Li, Q., Zhu, Y., Shangguan, W., Wang, X., Li, L., and Yu, F.: An attention-aware LSTM model for soil moisture and soil temperature prediction, Geoderma, 409, 115651, https://doi.org/10.1016/j.geoderma.2021.115651, 2022.

Li, X., Zhu, Y., Li, Q., Zhao, H., Zhu, J., and Zhang, C.: Interpretable spatio-temporal modeling for soil temperature prediction, Front. For. Glob. Change, 6, 1295731,

https://doi.org/10.3389/ffgc.2023.1295731, 2023a.

Li, X., Zhang, L., Wang, X., and Liang, B.: Forecasting greenhouse air and soil temperatures: A multi-step time series approach employing attention-based LSTM network, Comput. Electron. Agric., 217, 108602, https://doi.org/10.1016/j.compag.2023.108602, 2024c.

Li, Y., Zeng, H., Zhang, M., Wu, B., Zhao, Y., Yao, X., Cheng, T., Qin, X., and Wu, F.: A county-level soybean yield prediction framework coupled with XGBoost and multidimensional feature engineering, Int. J. Appl. Earth Obs. Geoinformation, 118, 103269, https://doi.org/10.1016/j.jag.2023.103269, 2023b.

Liu, F., Wu, H., Zhao, Y., Li, D., Yang, J.-L., Song, X., Shi, Z., Zhu, A.-X., and Zhang, G.-L.: Mapping high resolution National Soil Information Grids of China, Sci. Bull., 67, 328–340, https://doi.org/10.1016/j.scib.2021.10.013, 2022.

Liu X., Li Z.-L., Duan S.-B., Leng P., and Si M.: Retrieval of global surface soil and vegetation temperatures based on multisource data fusion, Remote Sens. Environ., 318, 114564, https://doi.org/10.1016/j.rse.2024.114564, 2025.

Liu, Y., Liu, X., Fu, Z., Zhang, D., and Liu, L.: Soil temperature dominates forest spring phenology in China, Agric. For. Meteorol., 355, 110141, https://doi.org/10.1016/j.agrformet.2024.110141, 2024.

Lloyd, J. and Taylor, J.: On the temperature dependence of soil respiration, Funct. Ecol., 315–323, https://doi.org/10.2307/2389824, 1994.

Loranty, M. M., Berner, L. T., Goetz, S. J., Jin, Y., and Randerson, J. T.: Vegetation controls on northern high latitude snow-albedo feedback: Observations and CMIP 5 model simulations, Glob. Change Biol., 20, 594 – 606, https://doi.org/10.1111/gcb.12391, 2014.

Mahanama, S. P. P., Koster, R. D., Reichle, R. H., and Suarez, M. J.: Impact of Subsurface Temperature Variability on Surface Air Temperature Variability: An AGCM Study, J. Hydrometeorol., 9, 804 – 815, https://doi.org/10.1175/2008JHM949.1, 2008.

Mo, Y., Pepin, N., and Lovell, H.: Understanding temperature variations in mountainous regions: The relationship between satellite-derived land surface temperature and in situ near-surface air temperature, Remote Sens. Environ., 318, 114574, https://doi.org/10.1016/j.rse.2024.114574, 2025.

Mortier, S., Hamedpour, A., Bussmann, B., Wandji, R. P. T., Latré, S., Sigurdsson, B. D., De Schepper, T., and Verdonck, T.: Inferring the relationship between soil temperature and the normalized difference vegetation index with machine learning, Ecol. Inform., 82, 102730, 2024.

Muñoz-Sabater, J., Dutra, E., Agustí-Panareda, A., Albergel, C., Arduini, G., Balsamo, G., Boussetta, S., Choulga, M., Harrigan, S., Hersbach, H., Martens, B., Miralles, D. G., Piles, M., Rodríguez-Fernández, N. J., Zsoter, E., Buontempo, C., and Thé paut, J.-N.: ERA5-Land: a state-of-the-art global reanalysis dataset for land applications, Earth Syst. Sci. Data, 13, 4349–4383, https://doi.org/10.5194/essd-13-4349-2021, 2021.

Myers-Smith, I. H., Elmendorf, S. C., Beck, P. S. A., Wilmking, M., Hallinger, M., Blok, D., Tape, K. D., Rayback, S. A., Macias-Fauria, M., Forbes, B. C., Speed, J. D. M., Boulanger-Lapointe, N., Rixen, C., Lévesque, E., Schmidt, N. M., Baittinger, C., Trant, A. J., Hermanutz, L., Collier, L. S., Dawes, M. A., Lantz, T. C., Weijers, S., Jørgensen, R. H., Buchwal, A., Buras, A., Naito, A. T., Ravolainen, V., Schaepman-Strub, G., Wheeler, J. A., Wipf, S., Guay, K. C., Hik, D. S., and Vellend, M.: Climate sensitivity of shrub growth across the tundra biome, Nat. Clim. Change, 5, 887–891, https://doi.org/10.1038/NCLIMATE2697, 2015.

Nahvi, B., Habibi, J., Mohammadi, K., Shamshirband, S., and Al Razgan, O. S.: Using self-adaptive evolutionary algorithm to improve the performance of an extreme learning machine for estimating soil temperature, Comput. Electron. Agric., 124, 150–160, https://doi.org/10.1016/j.compag.2016.03.025, 2016.

Ochsner, T. E., Horton, R., and Ren, T.: A new perspective on soil thermal properties, Soil Sci. Soc. Am. J., 65, 1641–1647, https://doi.org/10.2136/sssaj2001.1641, 2001.

Peng, S., Ciais, P., Krinner, G., Wang, T., Gouttevin, I., McGuire, A. D., Lawrence, D., Burke, E., Chen, X., Decharme, B., and others: Simulated high-latitude soil thermal dynamics during the past 4 decades, The Cryosphere, 10, 179–192, 2016.

Rahman, M. H. ur, Ahmad, A., Wajid, A., Hussain, M., Rasul, F., Ishaque, W., Islam, Md. A., Shelia, V., Awais, M., Ullah, A., Wahid, A., Sultana, S. R., Saud, S., Khan,

S., Fahad, S., Hussain, M., Hussain, S., and Nasim, W.: Application of CSM-CROPGRO-cotton model for cultivars and optimum planting dates: Evaluation in changing semi-arid climate, Field Crops Res., 238, 139 – 152, https://doi.org/10.1016/j.fcr.2017.07.007, 2019.

Shati, F., Prakash, S., Norouzi, H., and Blake, R.: Assessment of differences between near-surface air and soil temperatures for reliable detection of high-latitude freeze and thaw states, Cold Reg. Sci. Technol., 145, 86 – 92, https://doi.org/10.1016/j.coldregions.2017.10.007, 2018.

Smith, S. L., O'Neill, H. B., Isaksen, K., Noetzli, J., and Romanovsky, V. E.: The changing thermal state of permafrost, Nat. Rev. Earth Environ., 3, 10 – 23, https://doi.org/10.1038/s43017-021-00240-1, 2022.

Wan, Z. and Dozier, J.: A generalized split-window algorithm for retrieving land-surface temperature from space, IEEE Trans. Geosci. Remote Sens., 34, 892–905, https://doi.org/10.1109/36.508406, 1996.

Wang, D., Wang, A., and Wang, Z.: A multilayer daily high-resolution gridded homogenized soil temperature over continental China, Int. J. Climatol., 43, 2015–2030, https://doi.org/10.1002/joc.7959, 2023.

Wang, K. and Dickinson, R. E.: Contribution of solar radiation to decadal temperature variability over land, Proc. Natl. Acad. Sci., 110, 14877 – 14882, https://doi.org/10.1073/pnas.1311433110, 2013.

Wang, M., Wang, Y., Liu, X., Hou, W., Wang, J., Li, S., Zhao, L., and Hu, Z.: Vapor pressure deficit dominates vegetation productivity during compound drought and heatwave events in China's arid and semi-arid regions: Evidence from multiple vegetation parameters, Ecol. Inform., 88, 103144, https://doi.org/10.1016/j.ecoinf.2025.103144, 2025a.

Wang, Q., Tang, Y., Tong, X., and Atkinson, P. M.: Filling gaps in cloudy landsat LST product by spatial-temporal fusion of multi-scale data, Remote Sens. Environ., 306, 114142, https://doi.org/10.1016/j.rse.2024.114142, 2024.

Wang, X., He, L., Shi, H., and Yu, Q.: Daily multi-layer soil temperature dataset with 1 km resolution in China from 2010 to 2020,

https://doi.org/10.11888/Terre.tpdc.302333, 2025b.

Wu, P., Su, Y., Duan, S., Li, X., Yang, H., Zeng, C., Ma, X., Wu, Y., and Shen, H.: A two-step deep learning framework for mapping gapless all-weather land surface temperature using thermal infrared and passive microwave data, Remote Sens. Environ., 277, 113070, https://doi.org/10.1016/j.rse.2022.113070, 2022.

Xing, L., Li, L., Gong, J., Ren, C., Liu, J., and Chen, H.: Daily soil temperatures predictions for various climates in United States using data-driven model, Energy, 160, 430–440, https://doi.org/10.1016/j.energy.2018.07.004, 2018.

Xu, C., Qu, J. J., Hao, X., Zhu, Z., and Gutenberg, L.: Surface soil temperature seasonal variation estimation in a forested area using combined satellite observations and in-situ measurements, Int. J. Appl. Earth Obs. Geoinformation, 91, 102156, https://doi.org/10.1016/j.jag.2020.102156, 2020.

Xu, C., Liao, S., Huang, L., and Xia, J.: Soil temperature estimation at different depths over the central Tibetan Plateau integrating multiple Digital Earth observations and geo-computing, Int. J. Digit. Earth, 16, 4023 – 4043, https://doi.org/10.1080/17538947.2023.2264267, 2023.

Xu, S., Fu, Q., Li, T., Meng, F., Liu, D., Hou, R., Li, M., and Li, Q.: Spatiotemporal characteristics of the soil freeze-thaw state and its variation under different land use types - A case study in Northeast China, Agric. For. Meteorol., 312, 108737, https://doi.org/10.1016/j.agrformet.2021.108737, 2022.

Yamamoto, Y., Ichii, K., Ryu, Y., Kang, M., and Murayama, S.: Uncertainty quantification in land surface temperature retrieved from Himawari-8/AHI data by operational algorithms, ISPRS J. Photogramm. Remote Sens., 191, 171–187, https://doi.org/10.1016/j.isprsjprs.2022.07.008, 2022.

Yang, K. and Zhang, J.: Evaluation of reanalysis datasets against observational soil temperature data over China, Clim. Dyn., 50, 317 – 337, https://doi.org/10.1007/s00382-017-3610-4, 2018.

Yang, Q., Xu, M., Liu, H., Wang, J., Liu, L., Chi, Y., and Zheng, Y.: Impact factors and uncertainties of the temperature sensitivity of soil respiration, Shengtai XuebaoActa Ecol. Sin., 31, 2301–2311, 2011.

You, W., Huang, C., Hou, J., Zhang, Y., Dou, P., and Han, W.: Reconstruction of MODIS LST Under Cloudy Conditions by Integrating Himawari-8 and AMSR-2 Data

Through Deep Forest Method, IEEE Trans. Geosci. Remote Sens., 62, 1–17, https://doi.org/10.1109/TGRS.2024.3388409, 2024.

Zhang, T.: Influence of the seasonal snow cover on the ground thermal regime: An overview, Rev. Geophys., 43, https://doi.org/10.1029/2004RG000157, 2005.

Zhang, Y., Chen, W., Smith, S. L., Riseborough, D. W., and Cihlar, J.: Soil temperature in Canada during the twentieth century: Complex responses to atmospheric climate change, J. Geophys. Res. Atmospheres, 110, https://doi.org/10.1029/2004JD004910, 2005.

Zhao, T., Liu, S., Xu, J., He, H., Wang, D., Horton, R., and Liu, G.: Comparative analysis of seven machine learning algorithms and five empirical models to estimate soil thermal conductivity, Agric. For. Meteorol., 323, 109080, https://doi.org/10.1016/j.agrformet.2022.109080, 2022.